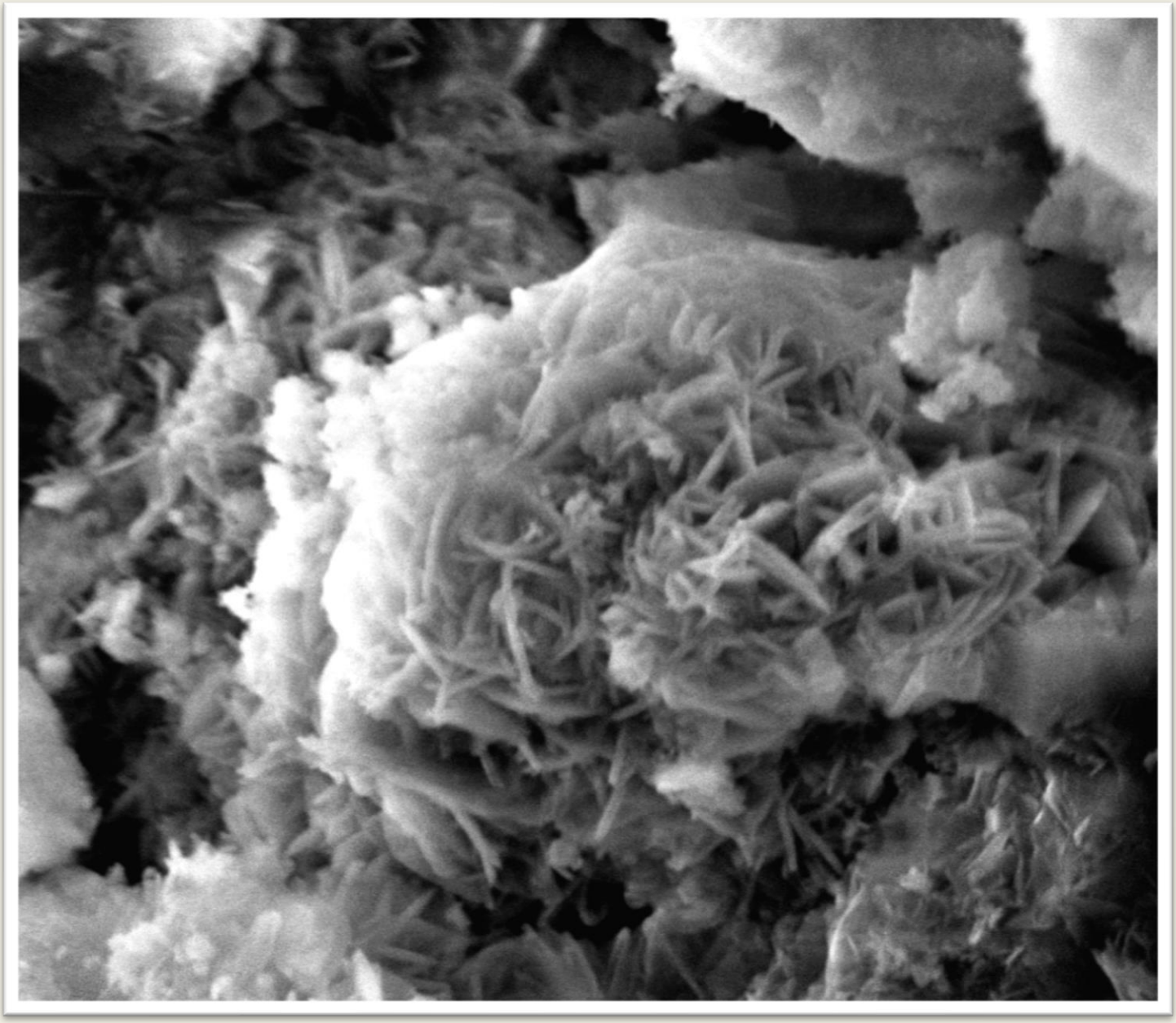

Degradation of model biomedical Mg alloys in aqueous media

Max Viklund

Division of Materials Engineering

Department of Mechanical Engineering

Master's Thesis 2019

LUNDS UNIVERSITET

Degradation of model biomedical Mg alloys in aqueous media

Master's Thesis

by

Max Viklund

Division of Materials Engineering

Department of Mechanical Engineering
Lund University, January 2020

Examiner: Professor Aylin Ahadi
Supervisor: Professor Dmytro Orlov
Co-supervisor: Professor Lars Wadsö

Front-page picture: SEM image of corroded Mg-alloy by Max Viklund

Division of Materials Engineering
Department of Mechanical Engineering, LTH
Ole Römers väg 1
P. O. Box 118
SE-221 00, Lund, Sweden,

Tel: +46 46 222 8505

MSc Thesis
ISRN LUTFD2/TFMT--20/5063--SE

Department of Mechanical Engineering
Lund University
Box 118
SE-22100 Lund
Sweden

Printed in Sweden
Lund 2020

Acknowledgements

Firstly I would like to thank my examiner Aylin Ahadi for taking the time to watch my presentation, and correct my report, as well as my supervisor Professor Dmytro Orlov, and effective co-supervisor Lars Wadsö for their help and support in this project. Whenever I got stuck I never felt afraid to ask for help, and it has been a pleasure to work with you.

I would also like to thank Elis Sjögren-Levin and all the other wonderful people at the Department of Mechanical Engineering that I met during my time here, who welcomed me without hesitation.

This project would not have happened without all of my amazing friends I've made during my time at Lund University, as I don't think I would have made it this far if they were not around.

Finally I want to thank my mother and father, Karen Meyer and Lars Viklund, who have always supported me in all my efforts, whether academic or not. I could not have asked for better parents.

Thank you.

Max Viklund
January 2020

Abstract

This project investigates the influence of alloying elements, heat treatment and corrosion medium on the corrosion rates of three magnesium alloys Mg-5Zn, Mg-0.27Ca, and Mg-0.27Ca-5Zn for use in bio-medical applications. A new method combining isothermal calorimetry and pressure measurements was used as a prime experimental tool in this investigation.

Material samples were tested in a physiological 0.9 wt.% NaCl solution and modified simulated body fluid (m-SBF) that mimic the concentrations of Cl^- and other ions in human blood plasma.

Corrosion resistance generally improves with the material heat treatment when super-saturated solid solution is formed, and corrosion medium promotes passivation of a protective film from degradation products. For instance, Mg-5Zn alloy in m-SBF exhibits the lowest corrosion rate. The level of the solution pH also affects the kinetics of corrosion reaction, but the effect depends on a specific material composition.

Sammanfattning

Detta projekt undersöker inflytandet av legeringskomposition, korrosionsmedium, och värmebehandling på korrosionshastigheten av tre magnesiumlegeringar; Mg-5Zn, Mg-0.27Ca, and Mg-0.27Ca-5Zn, för användning inom biomedicinska tillämpningar. En ny metod som kombinerar isoterm kalorimetri med tryckmätningar var det huvudsakliga mätinstrumentet som tillämpades i denna undersökning.

Materialprover testades i fysiologisk 0.9 v-% NaCl-lösning och modified simulated body fluid (m-SBF), som har motsvarande jonkoncentrationer som mänsklig blodplasma.

Korrosionsbeständighet ökade generellt med värmebehandling då en supermättad fast lösning uppstår, och korrosionsmedium främjar passivering genom en skyddande film bestående av degraderingsprodukter. Till exempel, Z5-legering i m-SBF uppvisade lägst korrosionshastighet. Värdet av pH i testlösningen visades påverka korrosionsprocessens reaktionskinetik, men effekten skilde sig mellan de olika legeringskompositionerna.

Populärvetenskaplig sammanfattning

Magnesium är en metall med många intressanta egenskaper. Med hänsyn till sin lätta vikt, och relativt låga pris har magnesium länge varit intressant ur ett materialperspektiv. Det stora hindret för tillämpningen av magnesium som konstruktionsmaterial är dess dåliga korrosionsbeständighet, d.v.s. magnesium reagerar med både luft och vatten och bryts ned väldigt lätt. Med det i åtanke har en ny typ av biomedicinska implantat för behandling av benbrott, tillverkade i magnesium, börjat undersökas. Magnesium är väldigt biokompatibelt; det är inte giftigt eller skadligt i människokroppen, och löser upp sig fort. Dagens implantat, ofta gjorda av stål eller titan, måste opereras ut igen efter det att benet läkt. Dessa magnesium-baserade implantat skulle lösas upp allt eftersom benvävnaden växer tillbaka, och därmed undvika riskerna och kostnaderna associerade med den andra operationen.

Rent magnesium löser dock upp sig för fort, och försvinner innan skadan har hunnit läka. Därmed undersöktes olika metoder för att påverka korrosionshastigheten i detta projekt. Dels undersöktes olika legeringar, d.v.s. blandningar av magnesium med andra metaller, i detta fall zink och kalcium. Dessa metaller är precis som magnesium ekonomiska och biokompatibla. Inverkan av legeringarnas så kallade mikrotillstånd på korrosionshastighet undersöktes också.

När en legering gjuts bildas mikroskopiska regioner av olika kompositioner i metallen. Dessa regioner agerar i praktiken som elektroder, och bildar massvis av små batterier, och påskyndar korrosionsreaktionen. Genom att värma upp legeringen till en viss temperatur så löser dessa regioner upp sig, och resultatet är ett homogent material, som i teorin borde uppvisa bättre korrosionsbeständighet.

Eftersom planen är att tillämpa dessa material som implantat, är det relevant att testa dem under förhållanden liknande de i kroppen. Därmed togs två olika testlösningar fram; en lösning med 9 vikt-procent NaCl, vilket används som en standard inom biomedicinsk forskning, och *simulated body fluid*, som härmar jonhalterna i blodplasma.

När magnesium korroderar frigörs värme och vätgas. Om två prov placeras i en kalorimeter, ett prov där reaktionen sker och ett utan, kan mängden värme mätas. Kalorimetern håller båda proven vid samma temperatur, så effekten som krävs för att kyla det reagerande provet är lika med värmen som frigörs. Om trycket av den frigjorda vätgasen mäts kan mängden av reagerat magnesium beräknas. Kombinationen av dessa två metoder utgör grunden för analysen av provens korrosionsegenskaper i detta projekt.

Glossary with abbreviations

ΔH: Reaction enthalpy

dn/dt: Corrosion rate

dp/dt: Pressure change rate

EDS: Energy-dispersive X-ray spectroscopy

MgO: Magnesium oxide

$Mg(OH)_2$: Magnesium hydroxide

m-SBF: modified Simulated Body Fluid

NaCl: Sodium chloride

SE: Secondary electrons

SEM: Scanning electron microscopy

X0: Mg-0.27Ca alloy (wt.%)

Z5: Mg-5Zn alloy (wt.%)

ZX50: Mg-0.27Ca-5Zn alloy (wt.%)

List of figures

Figure 1: Corrosion rate after 24h in NaCl for X0, ZX50, Z5 alloys (B. Reinwalt, I. Tayeb-Rey, 2019). 3
Figure 3: Schematic illustration of a solid solution treatment process. Cast specimen with solid precipitates (left) is heated until composition is homogeneous (right). 4
Figure 4: $Mg(OH)_2$ nano-flowers (D. Orlov, et al, 2019). Used with permission. 5
Figure 5: (Left): Original Pourbaix diagram of Mg-water system (Perrault, 1974), ... 5
Figure 6: Illustration of the overall structure after corrosion. Adapted from (Nordlien, 1997) .. 6
Figure 7: Comparison of corrosion rates in NaCl and m-SBF(B. Reinwalt, I. Tayeb-Rey, 2019). 7
Figure 7: (a) TAM Air isothermal calorimeter. (1-3) Three of the eight calorimeter channels. (4) Temperature regulator. (5) Peltier element. (6) Insulation. (7) Data-logger and power supply (Wadsö, L. 2005). (b) Schematic of the experimental setup with sample vial (s), reference vial (r), and gas collecting vial (g). Sample and gas collecting vials and pressure sensor are connected with stainless steel tubes (black lines). 9
Figure 8: Automatic diamond wire saw used for cutting specimens, with oil lubricant. 12
Figure 9: Loaded calorimeter with pressure sensors connected. 15
Figure 10: Cut and flared specimen for pH test. 16
Figure 11: FEI Quanta 200 Scanning electron microscope (SEM). 17
Figure 12: Original mounting system. Specimen is attached to the tip of the rod with UV-curing adhesive. 18
Figure 13: Version 1 of the holder as a) 3D model, and b) finished print holding specimen. 19
Figure 14: Version 2 of the holder a) as 3D-model, and b) mounted with sample in vial. 20
Figure 15: Secondary Electron SEM images of Z5 sample after exposure in NaCl solution for 7 days; a) Edge of sample, bulk metal indicated by arrow, b) face of sample (50x), c) face of sample (8000x). 21
Figure 16: Secondary Electron SEM image of Z5 alloy after exposure in m-SBF for 7 days. 22
Figure 17: a) Point analysis of bright spot on m-SBF submerged Z5 sample, b) XEDS results, showing composition of oxygen, magnesium, phosphorus, and calcium. 22
Figure 18: a) EDS line-scan of cross-section of Z5 alloy submerged in m-SBF for 7 days, b) results showing molar ratios of oxygen and magnesium, regions of approximate ratios of O to Mg indicated (dashed lines). 23
Figure 19: Thermal power and pressure change rate readings of X0, ZX50, and Z5 alloys in 0.9 w-% NaCl solution tested at 37°C for 48 hours (X0 only tested for approx. 20 hours). .. 24
Figure 20: Derivatives of the results in figure 19. Derivative of thermal power (solid lines), and pressure change rate (dotted lines). 24
Figure 21: Thermal power and pressure change rate readings of X0, ZX50, and Z5 alloys in m-SBF, tested at 37°C for 48 hours. 25
Figure 22: Derivatives of the results in figure 21. Derivative of thermal power (solid lines), and pressure change rate (dotted lines). 26
Figure 23: Thermal power and pressure change rate readings for heat treated X0, ZX50, and Z5 alloys in m-SBF, at 37°C for 48 hours. 26
Figure 24: Derivatives of the results in figure 23. Derivative of thermal power (solid lines), and pressure change rate (dotted lines). 27
Figure 25: Change in corrosion rates (a-c), and enthalpies (d-f) over time for as cast and SSSS X0, ZX50, and Z5 alloys tested in NaCl and SBF at 37°C for 48 hours. Enthalpies are

presented as absolute values, though as exothermic reaction enthalpies, they would be negative. 29
Figure 26: Corrosion rate for Z5, X0, and ZX50 as cast alloys in m-SBF, tested at 37°C for 140 hours. 30
Figure 27: Average corrosion rates of as cast and SSSS X0, ZX50, and Z5 alloys, tested in NaCl and SBF at 37°C after 24h. 31
Figure 28: Average corrosion rates of as cast and SSSS X0, ZX50, and Z5 alloys, tested in NaCl and SBF at 37°C after 48h (Data for X0 in NaCl not available). 32
Figure 29: a) evolution of pH factor of test medium, with pure Mg tested in NaCl solution, b) heat output of reaction of pure Mg in NaCl solution, with measured results (solid line), and extension of linear region (dashed line). 33
Figure 30: a) evolution of pH factor of test medium, with Z5 tested in NaCl solution at 37°C, b) heat output of reaction of Z5 in NaCl solution at 37°C, with measured results (solid line), and extension of linear regions (dashed lines). 34

Table of contents

Acknowledgements i
Abstract ii
Sammanfattning iii
Populärvetenskaplig sammanfattning iv
Glossary with abbreviations v
List of figures vi
Table of contents viii
1. Introduction 1
1.1 Overview 1
1.2 Aim 1
2. Background 2
2.1 Degradation of Mg 2
2.2 Effect of alloying elements 3
2.3 Solid solution treatment 3
2.4 Morphology of surface films 4
2.4.1 Mechanical stability 4
2.4.2 Chemical stability 5
2.4.3 Morphological effect of corrosion 6
2.5 Effect of corrosion medium 6
2.6 Isothermal calorimetry and pressure measurements 8
3. Method and materials 11
3.1 Sample preparation 11
3.2 Corrosion medium preparation 12
3.2.1 NaCl solution 12
3.2.2 m-SBF 13
3.3 Calorimeter setup 13
3.4 pH-measurements 15
3.5 Data analysis 16
3.6 Scanning Electron Microscopy (SEM) 16
4. Results & discussion 18
4.1 Sample mounting system 18
4.2 SEM and EDS analysis 21
4.2.1 Alloy Z5 after exposure in NaCl solution 21

4.2.2 Alloy Z5 after exposure in m-SBF 21
4.3 Calorimetry and pressure measurements 23
4.3.1 Exposure testing in NaCl solution 23
4.3.2 Exposure testing in m-SBF 25
4.3.3 Exposure testing of heat-treated specimens in m-SBF 26
4.3.4 Corrosion rates and enthalpies 27
4.3.5 Comparison of average corrosion rates 31
4.4 pH-levels and heat output 33
5. Conclusions 35
References 36
Appendix 1 37
Appendix 2 41

1. Introduction

1.1 Overview

Magnesium is a very lightweight material, the lightest among the structural metals (Aghion, E., Bronfin, B., 2000). As the eighth most abundant element in the Earth's crust it is relatively cheap, and posing low risks for the environment makes it a very sustainable material. These have led to a high interest in magnesium for its potential as a biomaterial (Esmaily et al., 2017).

The main biomedical application is as a degradable implant material. Screw and plate implants used to treat bone fractures at present are primarily made from titanium alloys or steels. Not only can these materials release toxic metal particles as they corrode, but due to their relatively high stiffness compared to natural bone, the surrounding bone tissue is weakened through a process known as "stress shielding". By contrast, magnesium has an elastic modulus much closer to that of bones, which mitigates this effect (Staiger et al., 2006).

The main barrier to overcome when it comes to magnesium implants, is excessively high degradation rate of magnesium in typical *in vivo* conditions. Significant amounts of hydrogen gas are released during corrosion process, which can damage the body tissues as pressure builds up (Witte et al., 2005). However if corrosion rate could be tuned to match that of bone regeneration, for instance through alloying, consuming magnesium alloy at a pace similar to the regrowth of bone tissue, second surgery for removing implants upon injury heal-up can be avoided. As surgery inherently carries many risks and costs, this would be very positive improvement.

Therefore, accurate measurement of corrosion rate in such materials is of great importance. This project employs the use of a new method under development in the divisions of 'materials engineering' and 'building materials' at LTH. This method combines traditional immersion testing with novel isothermal calorimetry and hydrogen pressure measurements.

1.2 Aim

The aims of this master's thesis are to use isothermal calorimetry and hydrogen gas pressure measurements to (i) examine calcium and zinc as efficient alloying elements for controlling the corrosion behaviour of magnesium in aqueous environments along with (ii) the effect of alloy solid solution treatment on corrosion rate; (iii) the influence of test solutions, 0.9% NaCl in water and simulated body fluid, on corrosion rate and surface morphology of corrosion products should also be studied.

2. Background

2.1 Degradation of Mg

Magnesium is a material with several interesting physical properties, but its use in practical applications have thus far been limited by particularly poor corrosion resistance. This is mainly due to two significant factors; i) degradation of magnesium alloys is special, in that Mg exhibits a high electro-negativity, which allows it to corrode even in the absence of oxygen, and ii) the resulting corrosion products on the surface offer little in passivation of the material bulk.

The corrosion properties of magnesium are generally dictated by two reactions; the oxidation of magnesium metal into MgO, and the hydroxylation of MgO into $Mg(OH)_2$. This reaction is exothermic, releasing heat, i.e. it has negative overall reaction enthalpy (ΔH).

Magnesium reacts readily with oxygen in the atmosphere and forms a thin layer of MgO according to reaction:

$$Mg(s) + ½O_2(g) \rightarrow MgO(s),\ \Delta H = -601.6\ kJ\ mol^{-1} \quad (1)$$

However,in aqueous environments magnesium reacts directly with water to form MgO, and a byproduct of this reaction is hydrogen gas:

$$Mg(s) + H_2O(l) \rightarrow MgO(s) + H_2(g),\ \Delta H = -315.41\ \ kJ\ mol^{-1} \quad (2)$$

Subsequently, hydroxylation of the MgO occurs, transforming it into $Mg(OH)_2$:

$$MgO(s) + H_2O(l) \rightarrow Mg(OH)_2(s),\ \Delta H = -37.6\ kJ\ mol^{-1} \quad (3)$$

Crucially, reaction 3 does not produce any hydrogen gas, which means that the amount of magnesium consumed during corrosion is directly proportional to the amount of hydrogen gas produced.

The overall reaction can then be written as:

$$Mg(s) + 2H_2O(l) \rightarrow Mg(OH)_2(s) + H_2(g),\ \Delta H = -353.01\ \ kJ\ mol^{-1} \quad (4)$$

Many metals have a naturally forming corrosion resistance, when corrosion products form a protective layer, which insulates the metal substrate from the electrolyte, impeding further breakdown. Both MgO and $Mg(OH)_2$ are insulators, and thus can protect the magnesium bulk from degradation. However, two fundamental weaknesses of the surface layers leading to their poor passivating abilities are mechanical and chemical instabilities (Esmaily et al., 2017).

2.2 Effect of alloying elements

In this project, three different magnesium alloys are to be examined, in weight percent: Mg-0.27Ca (X0), Mg-5Zn (Z5), and Mg-0.27Ca-5Zn (ZX50). Reinwalt and Tayeb-Rey (B. Reinwalt, I. Tayeb-Rey, 2019) found that all the alloys exhibit a lower corrosion rate than pure magnesium. Of the three tested alloys, Z5 had the highest corrosion rate, and X0 the lowest. ZX50 was in between, but much closer to that of X0 than Z5, see figure 1.

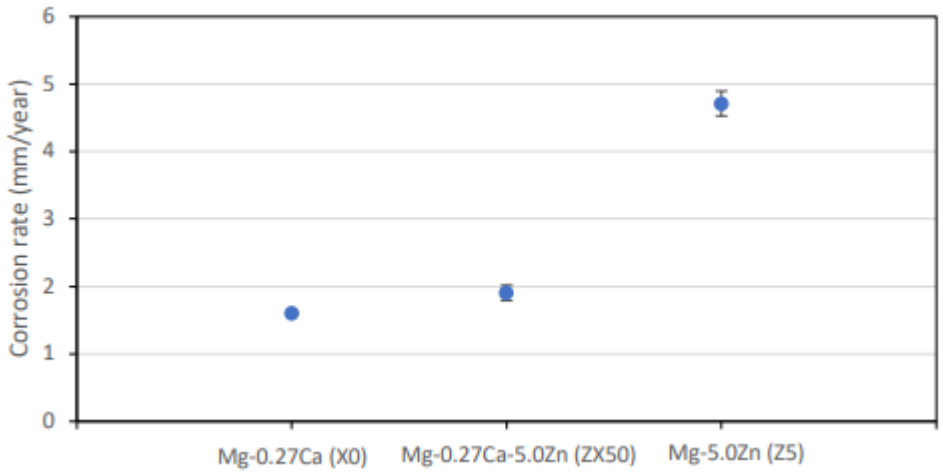

Figure 1: Corrosion rate after 24h in NaCl for X0, ZX50, Z5 alloys (B. Reinwalt, I. Tayeb-Rey, 2019).

2.3 Solid solution treatment

When a magnesium alloy is cast, different solid phases precipitate out as it cools. Primary precipitates form regions of local galvanic coupling increasing the rate of corrosion. During solid solution treatment the alloy is heated above a critical temperature where the primary precipitates dissolve into the matrix. The alloy is kept at this temperature for a sufficient time period to reach a homogeneous composition and is then rapidly cooled through quenching “locking” the microstructure, i.e. forming a super-saturated solid solution (SSSS) (Liu et al., 2018). This process is illustrated in figure 2.

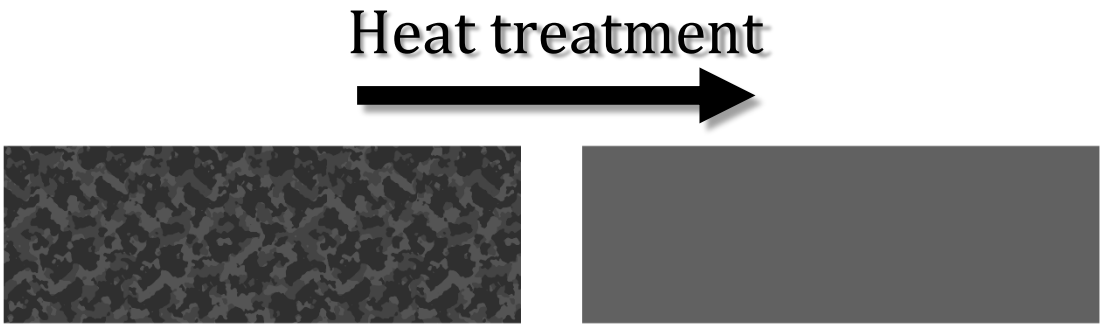

Figure 2: Schematic illustration of a solid solution treatment process. Cast specimen with solid precipitates (left) is heated until composition is homogeneous (right).

2.4 Morphology of surface films

2.4.1 Mechanical stability

A helpful metric in quickly assessing the potential passivating effect of a surface layer is so-called *Pilling-Bedworth ratio*, or PB ratio. The PB ratio is defined as the ratio between the molar volumes of surface film to that of a substrate (e.g. metal) bulk:

$$R_{PB} = \frac{V_{oxide}}{V_{metal}} \tag{4}$$

If a surface layer has a $1 < R_{PB} < 3$, it is under compression and is generally stable offering a good corrosion protection to the underlying metal. If the ratio is below 1, the oxide is under tension, porous and prone to crack-formation. If it is above 3, surface layer may crack under stress and flake off. These cracks will then allow electrolyte to make contact with the metal and corrosion continues.

Mg – MgO has $R_{PB} = 0.81$, i.e. MgO film tends to crack and thus offers little corrosion protection. Furthermore, MgO is soluble in water. On the other hand, Mg – $Mg(OH)_2$ has $R_{PB} = 1.77$. By dividing the R_{PB} for $Mg/Mg(OH)_2$, with the R_{PB} for Mg/MgO, the $R_{PB} = 2.19$. This suggests that it would form a robust, passivating layer. However, in this case the PB ratio is insufficient when evaluating any potential passivating effects. $Mg(OH)_2$ forms large porous networks of plate-like crystals. These pores act as channels guiding electrolyte towards magnesium metal surface, and as such $Mg(OH)_2$ does not offer good protection either (Ghali, 2011). These structures are sometimes referred to as *nano-flowers*, and an example of these can be seen in figure 3.

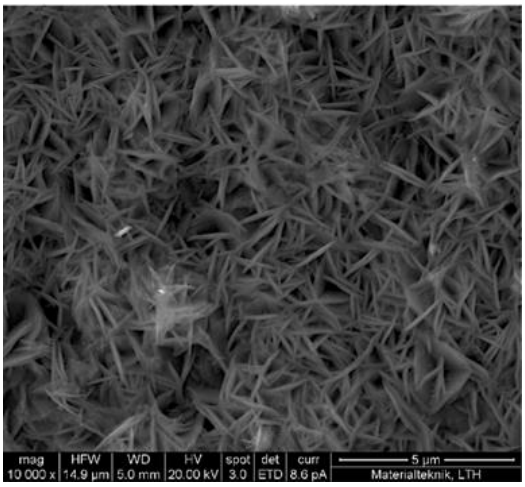

Figure 3: $Mg(OH)_2$ nano-flowers (D. Orlov, et al, 2019). Used with permission.

2.4.2 Chemical stability

The stability of corrosion products is highly dependent on electric potential and the acidity, or pH factor, of the solution. There are specific regions of potential and pH where certain products are stable and are not. This is the best expressed with an E-pH, or *Pourbaix*, diagram, as can be seen in figure 4 below.

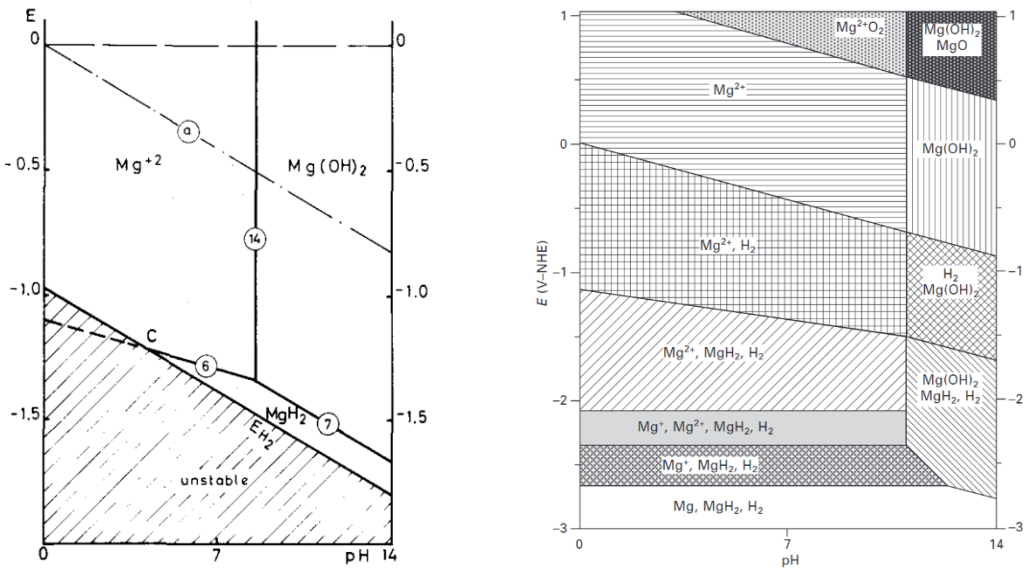

Figure 4: (Left): Original Pourbaix diagram of Mg-water system (Perrault, 1974), (Right): Expanded Pourbaix diagram (Song, 2011).

As seen in figure 4, $Mg(OH)_2$ is only stable in basic environments. That would mean that no $Mg(OH)_2$ layer would form in a neutral (pH~7) aqueous solution, instead dissociating into Mg^{2+} and $(OH)^-$ ions. As corrosion continues, the concentration of $(OH)^-$ ions in the solution steadily increase raising the alkalinity of the environment until a critical concentration is reached, and $Mg(OH)_2$ will no longer dissolve instead precipitating and growing on the metal surface (Ghali, 2011).

2.4.3 Morphological effect of corrosion

The effects described in section 2.4.1 and 2.4.2 combine during the degradation of magnesium in aqueous environments and result in a complex structure with many different layers. The bulk is pure Mg metal, which transitions into a hydrated cellular inner layer of $Mg(OH)_2$. Then, there is a thin layer of MgO, on top of which the plate-like $Mg(OH)_2$ grows. A schematic of the overall structure is illustrated in figure 5.

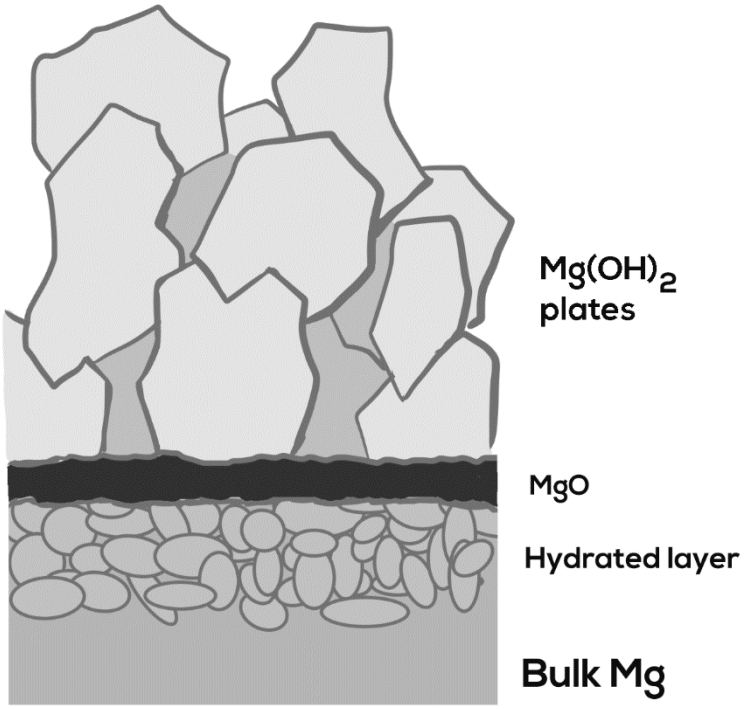

Figure 5: Illustration of the overall structure after corrosion.

2.5 Effect of corrosion medium

In this project, two corrosion media are used; a 0.9 w-% NaCl solution, which has the same concentration of chloride ions as human blood plasma and is widely used as a standard testing solution in biomedical research, and *Simulated Body Fluid* (SBF). SBFs are a group of solutions which mimic the ion concentrations in blood plasma, not just chloride. Therefore they are a more realistic substitute for actual blood plasma and are widely used for *in vitro* studies of biomedical alloys (Oyane et al., 2003). Different versions of SBF have been formulated, while for this study *modified simulated body fluid* (m-SBF) is selected.

Two main factors affect the corrosion rate of Mg alloys in NaCl. These include the lack of buffering salts leading to a steadily climbing of pH in the solution until $Mg(OH)_2$ stabilises and starts precipitating on the surface, as described in section 2.4.2, and the

presence of chloride-ions that have been proven to affect adversely Mg corrosion resistance (Song, 2011).

One of the main differences then with corrosion in m-SBF compared to NaCl is the presence of buffering salts that prevent the test solution from reaching the alkalinity required for $Mg(OH)_2$ to form. When considering reaction (4), this would accelerate the consumption of magnesium, resulting in a higher corrosion rate. The specimen would also lack the semi-protective layer of $Mg(OH)_2$ plates further increasing the rate of corrosion.

However, the presence of ions such as Ca^{2+} and PO_4^{3-} can react to form apatite on the metal surface. Apatite are a group of phosphate minerals found in natural bone. They have been shown to form a protective layer halting corrosion (Shuai et al., 2017). Predicting corrosion behaviour in m-SBF is therefore much more complicated than in the case of NaCl.

Xin et al. compared the corrosion rate of magnesium alloys in NaCl, SBF, Hank's solution, PBS, and DMEM and found that the rate of degradation was considerably higher in SBF than in NaCl (Xin, Hu and Chu, 2010).

When comparing corrosion rates in NaCl and m-SBF in Reinwalt & Tayeb-Rey report, figure 6, it can be seen that corrosion rates are higher in m-SBF for the X0 and ZX50 alloys but is considerably lower in the Z5 alloy.

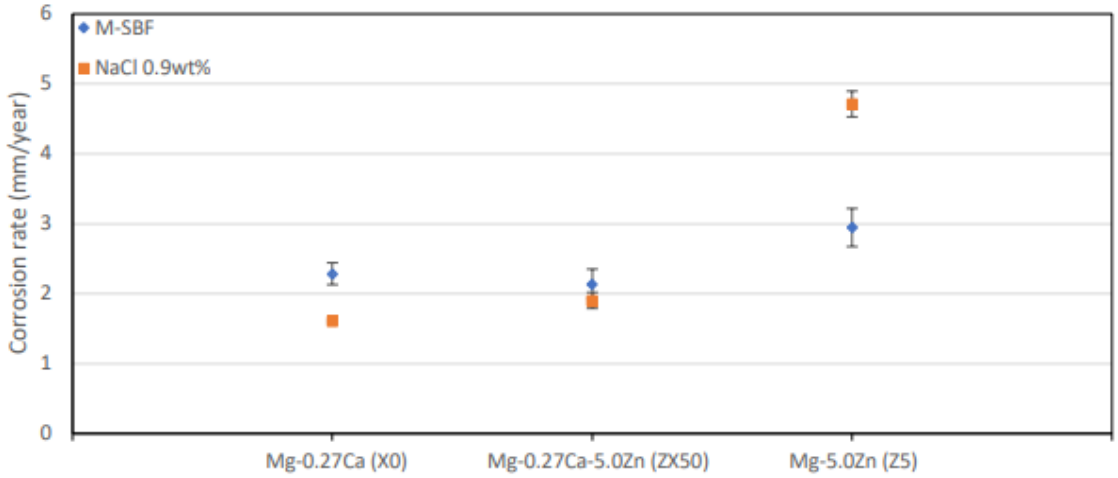

Figure 6: Comparison of corrosion rates in NaCl and m-SBF(B. Reinwalt, I. Tayeb-Rey, 2019).

2.6 Analytical techniques

2.6.1 Isothermal calorimetry and pressure measurements

The primary analytical instrument used in this project is an isothermal calorimeter connected to pressure sensors. An isothermal calorimeter consists of two chambers, one loaded with the sample, and a reference, see figure 7a. As the corrosion process takes place, it releases heat. The calorimeter keeps the sample and the reference chamber at a constant temperature, and the thermal power required to maintain the temperature in the sample chamber is proportional to the rate of corrosion according to equation:

$$P = \frac{dn}{dt} \cdot \Delta H \tag{5}$$

where P is thermal power (W), dn/dt is the corrosion rate of magnesium, and ΔH is the reaction enthalpy. The calorimeter records thermal power over time.

According to reaction 2, for every mole of Mg consumed one mole of H_2 is produced. This means that the corrosion of magnesium can be directly linked to the formation of hydrogen gas. By using the ideal gas law, the corrosion rate of magnesium can be correlated to the pressure change rate of hydrogen gas through equation:

$$\frac{dn}{dt} = \frac{dp}{dt} \cdot \frac{V}{RT} \tag{6}$$

where dn/dt is the corrosion rate of magnesium, dp/dt is the pressure change rate of hydrogen gas, V is the total gas volume of the system, R is the gas constant, and T is temperature. The advantage of this method of corrosion rate determination, over for instance conventional electrodynamic measurements, is that a stable reading of the progress of the corrosion reaction can be made over time during immersion, while affecting the specimen as minimally as possible.

By collecting the produced hydrogen gas and measuring pressure change over time, corrosion rate can be calculated. Figure 7b shows a schematic of the complete pressure measurement setup when placed in the calorimeter.

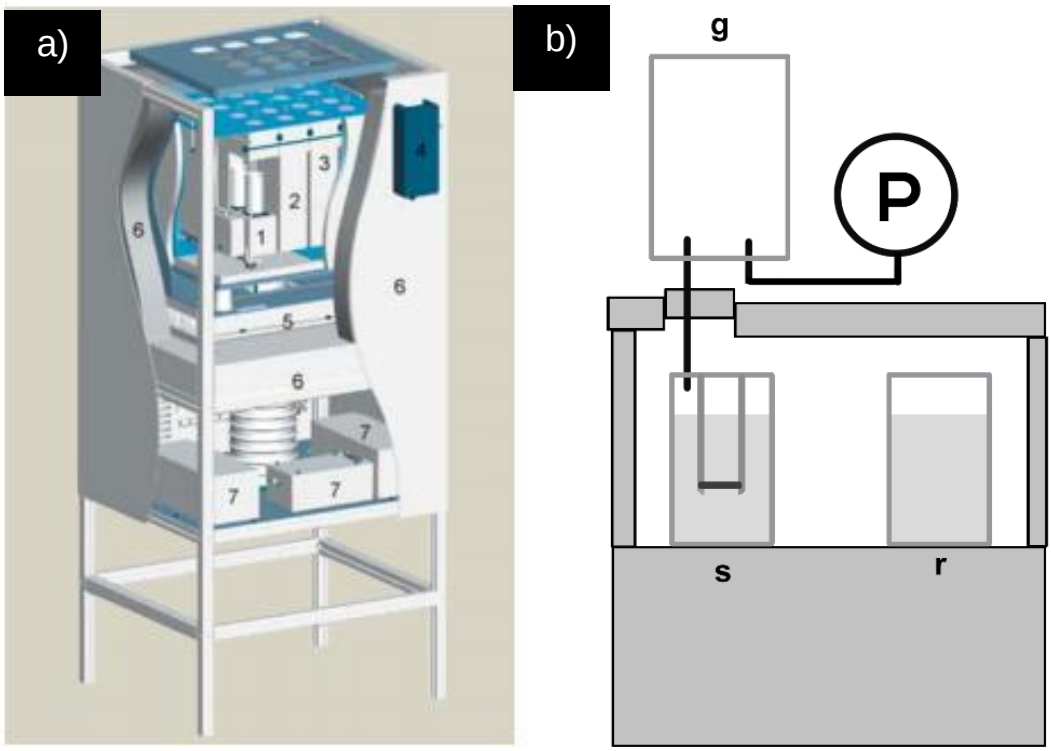

Figure 7: (a) TAM Air isothermal calorimeter. (1-3) Three of the eight calorimeter channels. (4) Temperature regulator. (5) Peltier element. (6) Insulation. (7) Data-logger and power supply (Wadsö, L. 2005). (b) Schematic of the experimental setup with sample vial (s), reference vial (r), and gas collecting vial (g). Sample and gas collecting vials and pressure sensor are connected with stainless steel tubes (black lines).

2.6.2 Measuring pH-levels

The pH of a solution is an indication of its acidity, which can affect reactions in various ways. As such it is often of interest to monitor how the pH of a test solution behaves in order to gain a more complete picture of the mechanisms at play. The pH level can be measured in a variety of ways, such as through titration or indicator paper, but the most convenient method, and the one used in this project, is a digital pH-meter. The pH-meter is equipped with an electrode that is directly submerged in the testing solution, which allows for continual recording of the levels throughout the reaction without disturbing the experimental setup. The pH-meter even accounts for the shift in pH that is associated with a change in temperature.

2.6.3 Scanning Electron Microscopy (SEM)

Electron microscopy is an advanced technique which can be used to image samples. Unlike “conventional” microscopy, which uses visible light, a scanning electron microscope (SEM), like its name implies, utilizes a beam of electrons instead, which is scanned over the surface. Since electrons have a much shorter wavelength than

visible light, a much higher resolution can be achieved, allowing for very minute details of surfaces to be imaged.

There are several different types of electron detectors used to capture the image in an SEM, which will affect which type of contrast is seen in the final picture. The two main contrasts are mass contrast, where heavier elements appear brighter, and topological contrast, which is analogous to regular black-and-white photography.

Most electron microscopes are also equipped with X-ray detectors which can be used to identify and quantify the elemental composition of the specimen. When the electron beam interacts with the specimen, some energy is lost to the atoms of the specimen. This energy loss is due to electrons in those atoms getting excited to a higher energy level. These electrons will then fall back down to their ground state, releasing a photon of X-rays in the process. The energy of that photon is characteristic of the type of element that atom is, and such can be used in order to identify the composition of the material. The number of X-rays of a certain wavelength emitted is proportional to the amount of each corresponding element. This is known as Energy Dispersive X-ray Spectroscopy (EDS).

3. Method and materials

3.1 Sample preparation

Two binary and one ternary magnesium alloys were tested in this project; Mg-5Zn containing 5 wt.% Zn, Mg-0.27Ca containing 0.27 wt.% Ca, and Mg-5Zn-0.27Ca containing 5 wt.% Zn, and 0.27 w-% Ca.

These specimens came in several states, and can be found in table 1:

Table 1: Specimens tested in this project; names, composition, and microstructure states listed.

Alloy Name, composition [wt.%]	Microstructure state	
Z5, Mg-5%Zn	As cast	-
	Heat treated	350°C, 12h
	Heat treated	420°C, 24h
X0, Mg-0.27%Ca	As cast	-
	Heat treated	450°C, 24h
ZX50, Mg-0.27%Ca-5%Zn	As cast	-
	Heat treated	450°C, 24h

Originally only one solid solution treatment was planned to be tested for each specimen, but as there was still time at the end of the project, an additional specimen of Z5, treated at a higher temperature, for a longer time, was tested.

The specimens were cut into squares approximately 9x9x1mm in size using a diamond wire saw in a water-free environment, as depicted in figure 8.

After cutting, each specimen was grinded on SiC paper in several steps down to 2000 grit. The specimen were rotated 90° between each grinding step decreasing the level of grit in order to remove the grooves from the preceding coarser grit. In order to minimize the formation of oxides, the last grinding step was performed in no more than one hour while as close to the start of the immersion experiment as possible.

After grinding the specimens, their dimensions were measured with a digital micrometer. Each side was measured five times in different places, then the minimal and maximum values were assumed to be outliers, and the averages of the remaining measurements were used to calculate to total surface area of each specimen.

Before mounting the specimens in the calorimeter, they were cleaned in ethanol in an ultrasonic cleaner and dried with ultra clean air.

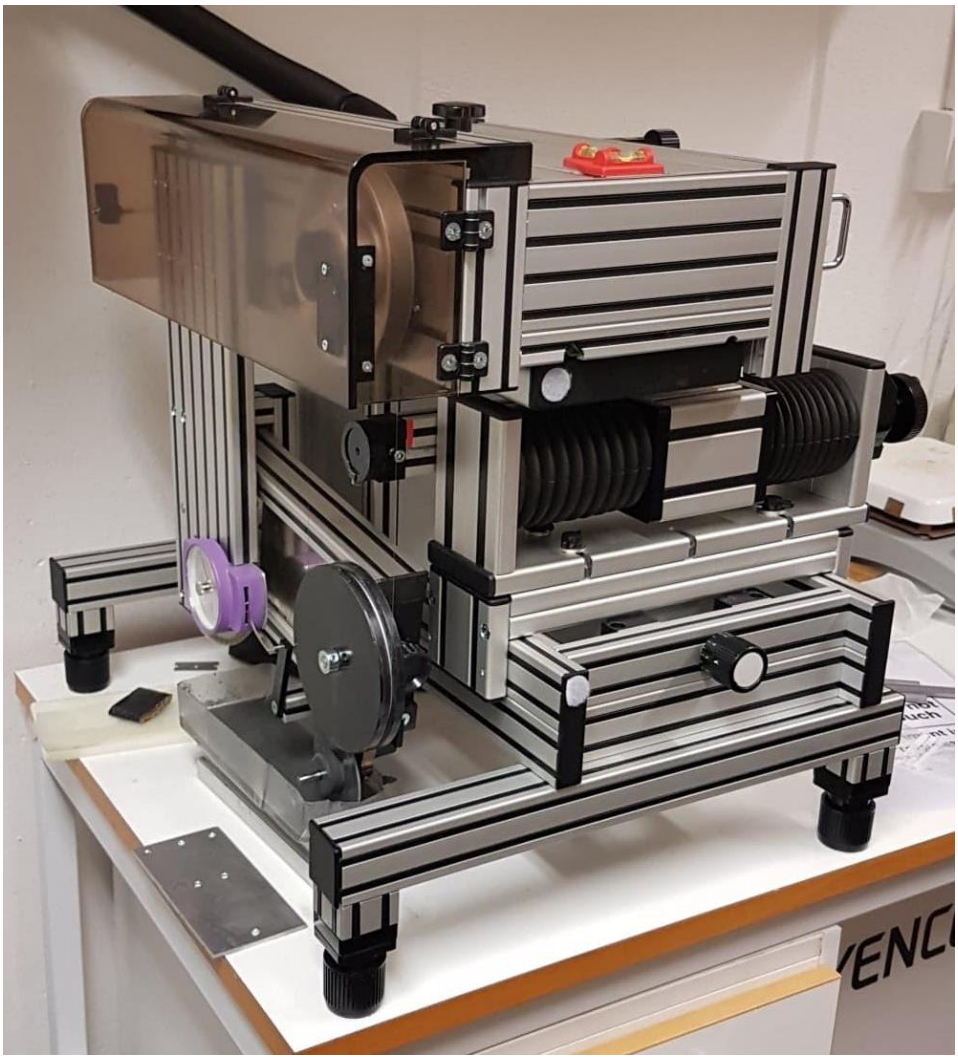

Figure 8: Automatic diamond wire saw used for cutting specimens, with oil lubricant.

3.2 Corrosion medium preparation

The corrosion properties of the samples were tested in two different solutions; 0.9 weight-% NaCl solution and *modified Simulated Body Fluid*, or m-SBF.

3.2.1 NaCl solution

The 0.9 w-% NaCl solution was prepared as follows:

- 100 mL of deionized water was poured into a 1000 mL beaker with a stir rod.
- 9 grams of NaCl was weighted and gradually added to the beaker.
- The beaker was filled with deionized water up to the 1000 mL gauge line while stirring.

3.2.2 m-SBF

The m-SBF solution was prepared as follows:

- 700 mL of deionized water was poured into a 1000 mL beaker with a stir rod on a heat plate.
- The water is brought to 37°C while stirring.
- These components were then added in their corresponding amounts:
    - 5.403 g of NaCl
    - 0.504 g of $NaHCO_3$
    - 0.426 g of Na_2CO_3
    - 0.225 g of KCl
    - 0.230 g of $K_2HPO_4 \cdot 3H_2O$
    - 0.311 g of $MgCl_2 \cdot 6H_2O$
    - 100 mL of 0.2M NaOH
    - 17.892 g of HEPES
    - 0.293 g of $CaCl_2$
    - 0.072 g of Na_2SO_4
    - 15 mL of 0.2M NaOH
- The pH was then adjusted to 7.37 with 0.2M NaOH
- The beaker was filled with deionized water up to the 1000 mL gauge line while stirring.
- The solution was left to cool down to room temperature.

3.3 Calorimeter setup

The calorimeter used in this project is the TAM Air by TA Instruments, (formerly Thermometric), equipped with eight channels. For this project, only four channels were used at a time, as that was the amount of pressure sensors available. The sensors in question were Motorola MPX5100. The calorimeter cover was also re-designed to accommodate the pressure measurements setup.

Using a PR-59 temperature controller, regulated by LT_Interface software from Laird Technologies, the temperature in the calorimeter was set to 37°C, matching the average body temperature in humans. The calorimeter has a limit of detection of 8 µW, according to the manufacturer (Wadsö, L. 2005).

First, four glass vials 20 mL were prepared by filling them with 17 mL of corrosion medium, (NaCl or m-SBF, depending on the experiment). These were topped with rubber stoppers and placed in the reference channels in the calorimeter. Then four identical vials were prepared, again with 17 mL of the corresponding corrosion medium. The vials were then connected to a corresponding larger vial via a thin steel tube, through the rubber stoppers.

These vials collect hydrogen gas that is generated during magnesium corrosion reaction. These larger vials are subsequently connected to the pressure sensors.

The four assembled sample vials were then wiped clean of any potential liquid residue on their surfaces that could affect the results, and then placed in the calorimeter. A piece of foam, with a channel cut to accommodate for the steel tube, was placed over the vials to insulate them. Figure 10 shows the complete, loaded calorimeter. The calorimeter lid was then closed, and two weights were placed on top to keep everything secure. At this point, the samples ***were not loaded into the calorimeter***. The corrosion reaction is highly temperature dependent. As such, the calorimeter was left for approximately an hour to let everything inside reach equilibrium. During this waiting period the final polishing step and sonication of the samples were performed, see section 3.1.

After everything was up to temperature, each vial was carefully but swiftly removed one by one from the calorimeter and mounted with the corresponding specimen using a 3D-printed holder that suspends the specimen in the solution. The lid of the calorimeter was replaced during the mounting to ensure as little heat loses as possible. Once all samples had been mounted in the calorimeter and connected to the pressure sensors the experiment was initiated. The software used to record the data was the PicoLog PLW Recorder and run on a separate laptop connected to both the calorimeter and pressure sensors. The software automatically logs changes in voltage over time from the instruments and saves the data as .PLW files.

Figure 9: Loaded calorimeter with pressure sensors connected.

3.4 pH-measurements

It is known that the pH of the solution affects the corrosion properties of the alloy. Therefore, it was decided to examine the evolution of pH with a reference sample subjected to the same conditions as in the experiments.

A sample of magnesium alloy was prepared the same way as described in section 3.1. Since vials were too narrow to accommodate both the pH-electrode and a sample holder, the alloy specimen was cut with pliers halfway through, and the two “legs” were pried apart, see figure 10. This ensures that the majority of specimen surface was in contact with the corrosion medium.

Figure 10: Cut and flared specimen for pH test.

To monitor the pH level evolution, Orion 720a Plus pH-meter was used. 17 mL of corrosion medium and the pH electrode were added to a vial and placed in the calorimeter. The calorimeter was only used to keep the test running at 37°C and did not monitor any calorimetric data for this channel. Similarly to the other calorimetric tests, this setup was left to reach equilibrium before the alloy sample was added. Once the pH-meter was stable at around 6.9 the sample was placed in the vial and the changes in pH were recorded until it stabilised again.

No way to automatically record the data with the pH-meter was found, and as such an *ad hoc* setup was conceived. Using a laptop with a standard posable webcam pointed to the display of the calorimeter, a video call was setup to the office, so that the pH-meter could be consistently observed remotely. Time and pH were recorded and transferred to an Excel spreadsheet for analysis. Measurements are presented in Appendix 2.

3.5 Data analysis

As the PLW recorder program only records voltage differentials, the raw data must be processed in order to acquire relevant information. A MATLAB script was used to convert the .PLW files with calorimetric and pressure data to MATLAB readable format, and another script was then used to calculate thermal power, heat flux, pressure change, pressure change rate, corrosion rate, and enthalpy variation. The MATLAB script can be found in Appendix 1.

3.6 Scanning Electron Microscopy (SEM)

In order to examine the surface morphology of the samples after testing, SEM imaging and chemical analysis were utilized.

The microscope used in this project was a FEI Quanta 200, with EDAX Spectroscopy EDS system. The samples had one edge grinded down to open the cross-section of the surface layers, and then mounted in the microscope. Since corrosion layers were expected to be complex in shape but relatively uniform in composition, the samples

were mainly analysed with secondary electrons (SE), since topological contrast was of highest interest. Since corrosion products are electrical insulators, it was crucial to find an area with a relatively thin surface layer to avoid charging effects distorting the image.

In order to examine the chemical composition of the surface layers, EDS was used. Results from the EDS testing were processed in the TEAM™ EDS Analysis System by EDAX.

Figure 11: FEI Quanta 200 Scanning electron microscope (SEM).

4. Results & discussion

4.1 Sample mounting system

In the original experimental setup, the specimens used to be mounted in the calorimeter by attaching them to the tip of plastic rods with UV-curing epoxy adhesive. This system proved to be problematic. Not only is the UV laser and the adhesive itself harmful, but the entire setup was unstable, and the samples used to often detach from the rods during testing. The glue also inherently interferes with the experiment as the area covered with the adhesive does not make contact with the corrosive medium. This non-reactive area was not taken into consideration in the calculation therefore leading to the overestimate of the total surface area of the samples. The original mounting system is depicted in figure 12.

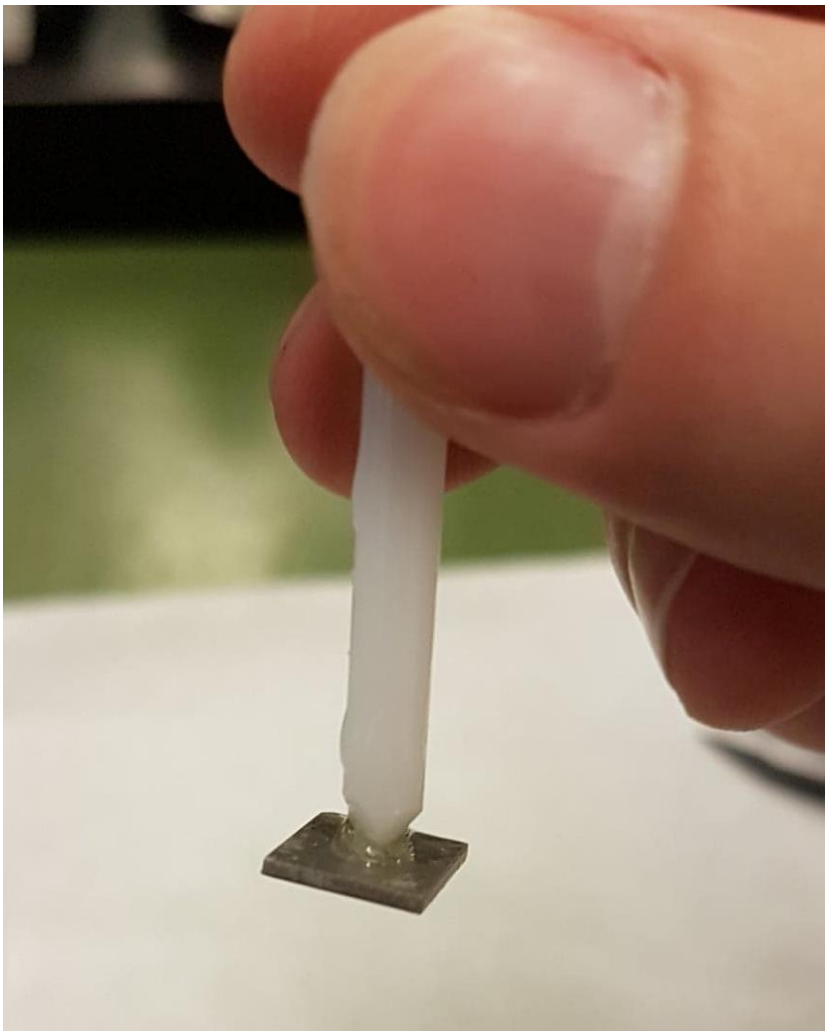

Figure 12: Original mounting system. Specimen is attached to the tip of the rod with UV-curing adhesive.

In order to address these issues, a mechanical holder was designed in 3D-modelling software and subsequently 3D-printed in PLA plastic. The first iteration was a V-shaped holder with teeth to hold the specimen. The sample is simply held in place between the prongs with tension.
Version 1 can be seen in figure 13.

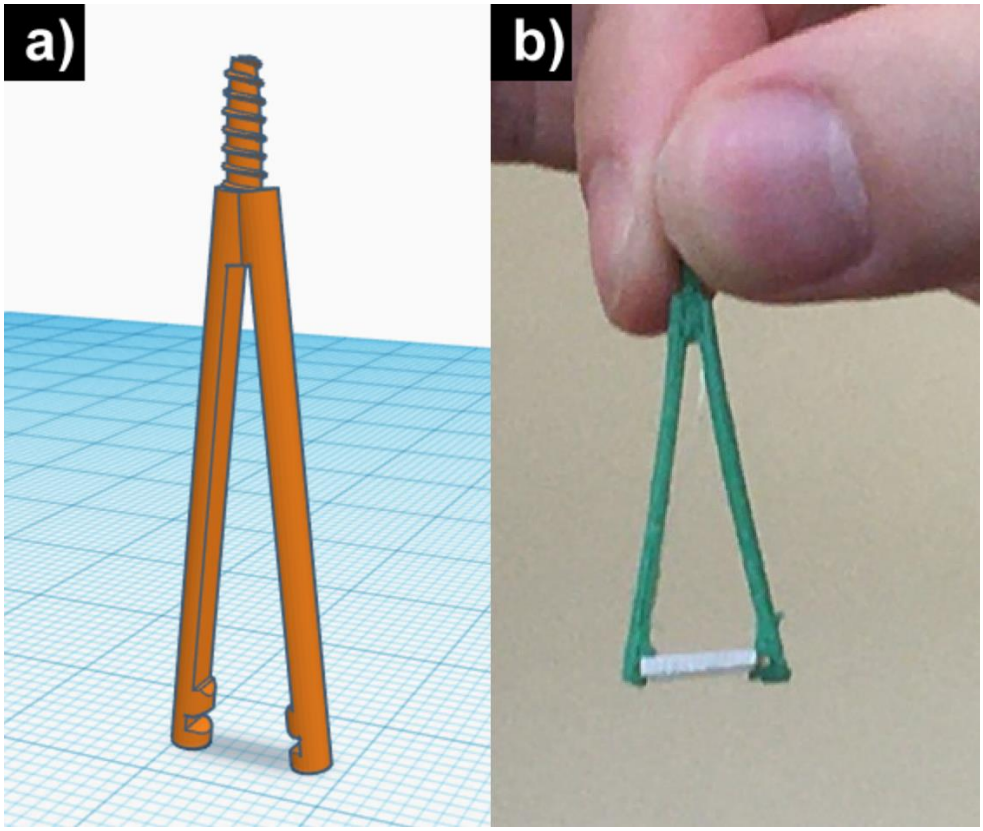

Figure 13: Version 1 of the holder as a) 3D model, and b) finished print holding specimen.

This holder, while much more efficient than the original setup, still was not satisfactory enough. Due to the stress it is subjected to while holding the specimen, the holder permanently deforms due to creep severely diminishing its grip strength after only a single experiment. As the holders were intended to be reusable, this was a considerable problem. While no apparent chemical effect on the holders was observed during the relatively short immersion periods, studies on the biocompatibility of PLA has shown the material to be degraded by NaCl (Lars' paper) and SBF over time (Barbeck et al., 2017).

To address these issues, revisions to the design were made. The entire holder was remodelled, this time with parallel prongs in order to minimize stress in the holder. The teeth were also modified in order to allow round specimens to be mounted both horizontally and vertically. The new holders were printed at Ingvar Kamprad Designcentrum (IKDC) in Lund, using *Selective Laser Sintering* (SLS), with a fine nylon powder. This technique allows a better printing resolution resulting in overall

higher-quality holders. While no studies on the degradation of nylon in SBF could be found, nylons are in general susceptible to acids, but resistant to pure water and alkaline solutions (UNITIKA Plastics Division, 2019). SBF is slightly basic, buffered to a pH of approximately 8.5. As such, these holders are more resilient than their PLA counterparts. Small amounts of hydroxyapatite can however start nucleating on nylon after prolonged immersion in SBF, which might affect the results (Waugh and Lawrence, 2010). Version 2 of the holder can be seen in figure 14.

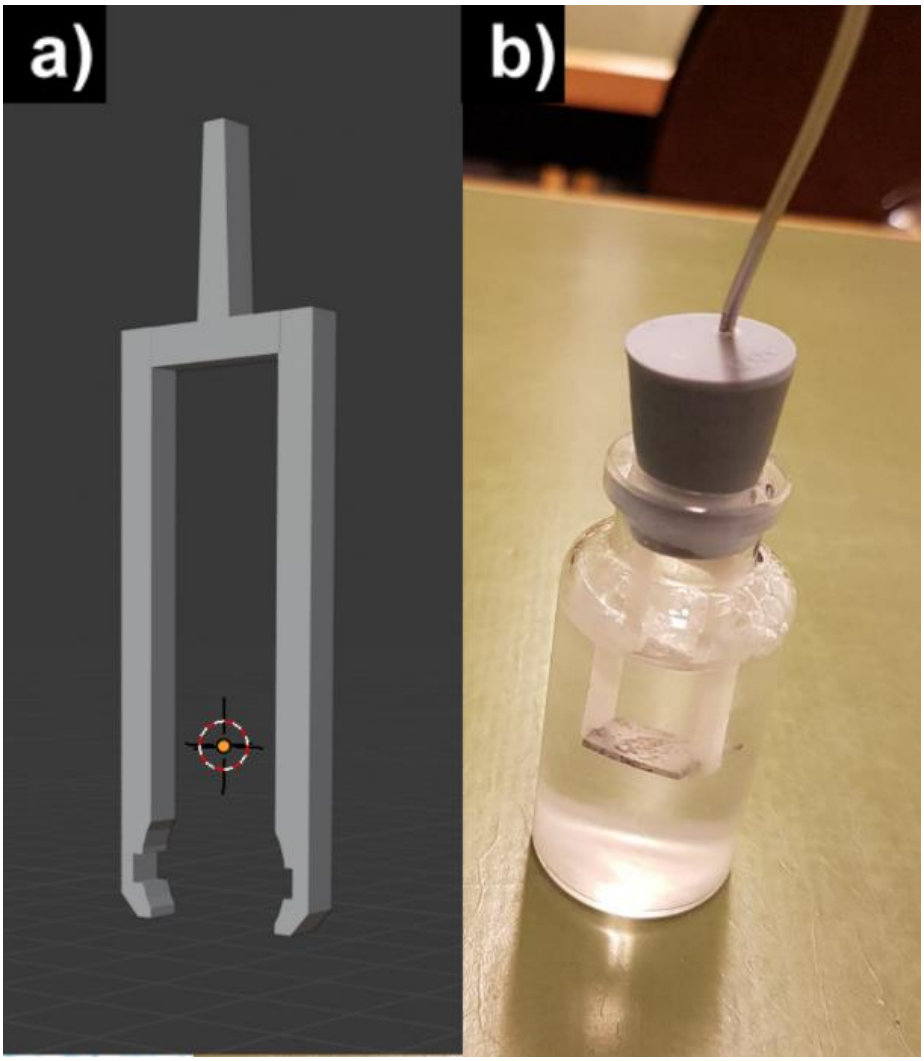

Figure 14: Version 2 of the holder a) as 3D-model, and b) mounted with sample in vial.

4.2 SEM and EDS analysis

4.2.1 Alloy Z5 after exposure in NaCl solution

After submersion for seven days, alloy Z5 sample is analysed with SEM, and extensive corrosive damaged can be observed throughout the entire sample surface. As seen in figure 15, the surface looks “sponge-like” with deep cavities extending into the sample. At higher magnification characteristic plate-like structures of $Mg(OH)_2$ become visible.

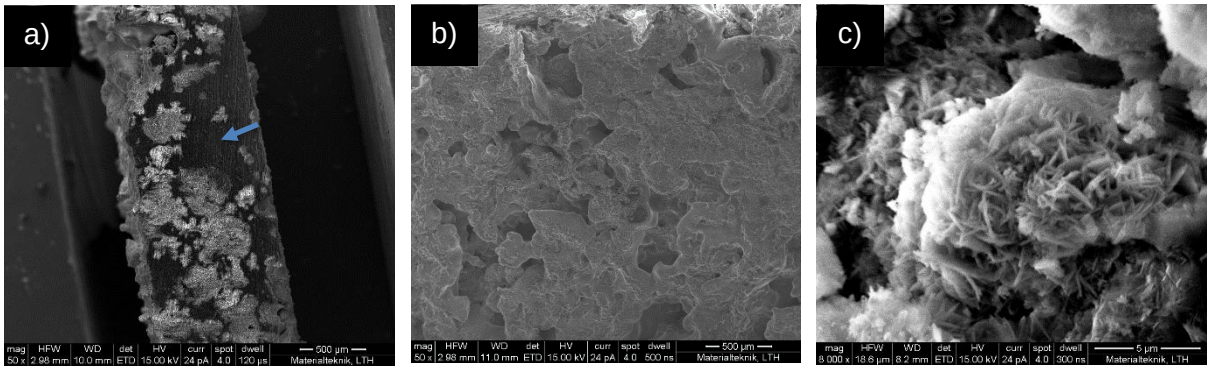

Figure 15: Secondary Electron SEM images of Z5 sample after exposure in NaCl solution for 7 days; a) Edge of sample, bulk metal indicated by arrow, b) face of sample (50x), c) face of sample (8000x).

EDS analysis of surface in figure 15b shows a composition of 2:1 molar ratio of oxygen to magnesium. This molar ratio would indeed suggest that the surface layer is $Mg(OH)_2$. EDS cannot detect hydrogen.

4.2.2 Alloy Z5 after exposure in m-SBF

The Z5 sample after exposure in m-SBF for seven days has a significantly different surface morphology than that in the sample exposed to NaCl. The surface exhibits a cracked pattern, with bright spots, see figure 18.

The appearance of cracks is consistent with expectations from a Pilling-Bedworth ratio below 1, which is the case for MgO. The plates of $Mg(OH)_2$ are not present, as expected since the buffering salts in m-SBF solution prevent the build-up of alkalinity required for $Mg(OH)_2$ formation.

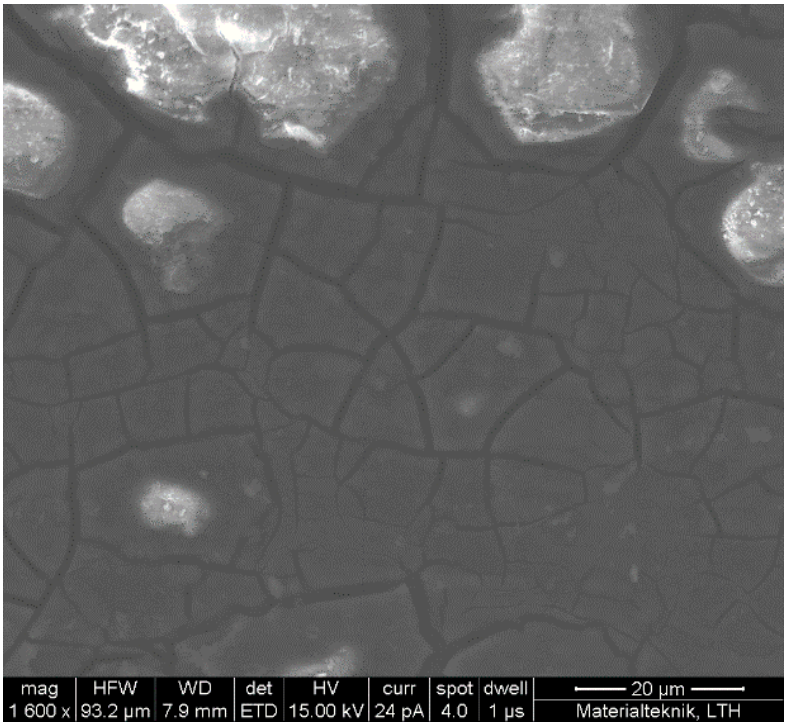

Figure 16: Secondary Electron SEM image of Z5 alloy after exposure in m-SBF for 7 days.

EDS analysis in figure 17 reveal that the bright spots are high in concentration of oxygen, calcium, and phosphorus, suggesting the presence of calcium phosphates, such as hydroxyapatite.

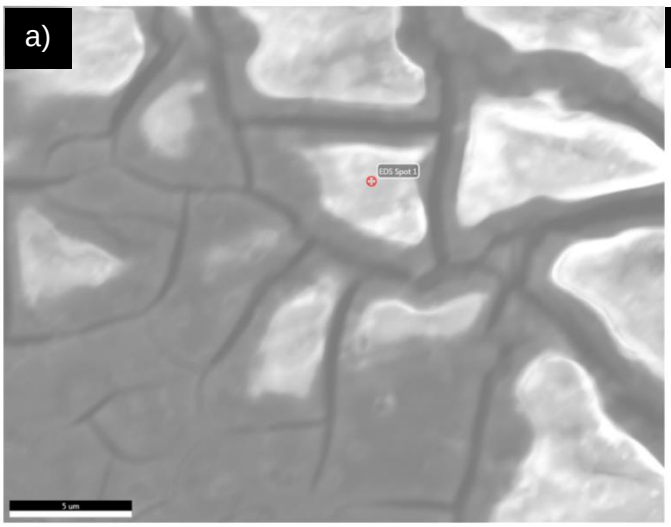

b)

eZAF Smart Quant Results

Element	Weight %	Atomic %	Net Int.
O K	50.87	66.93	26.19
MgK	14.61	12.65	11.14
P K	14.82	10.07	8.02
CaK	19.71	10.35	4.47

Figure 17: a) Point analysis of bright spot on m-SBF submerged Z5 sample, b) XEDS results, showing composition of oxygen, magnesium, phosphorus, and calcium.

The results of analysis of a specimen cross-section revealing the surface layers and an EDS line-scan are presented in figure 18. The bulk of the sample is nearly pure magnesium, while moving towards the edge the relative amount of oxygen starts to increase. Four distinct regions of specific molar ratios of oxygen to magnesium can be seen in the diagram, from left to right: pure magnesium, 2:1, near 1:1, and finally 2:1

oxygen to magnesium again. These correspond to the structure of bulk magnesium, hydrated inner layer, thin MgO layer, and $Mg(OH)_2$ on top, which is in agreement with that discussed in section 2.2.3.

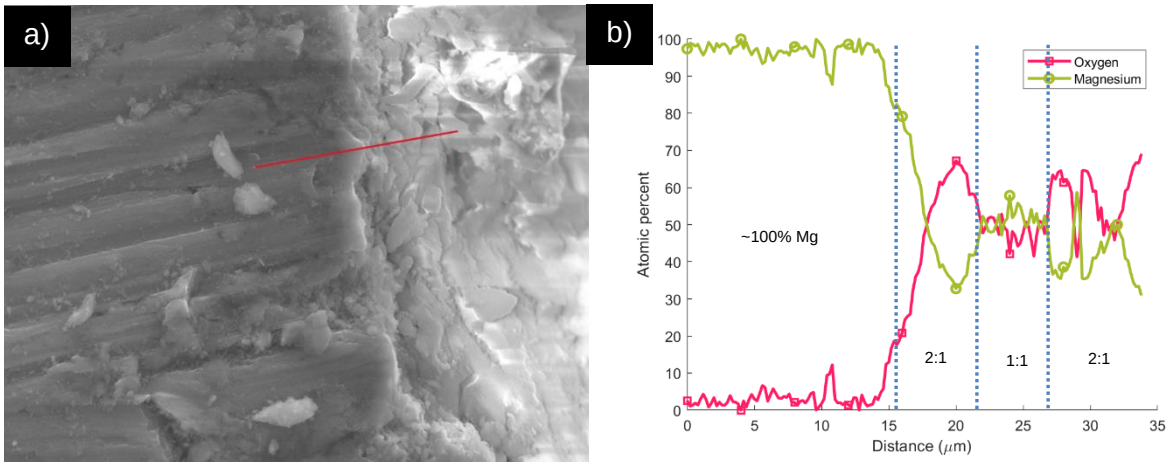

Figure 18: a) EDS line-scan of cross-section of Z5 alloy submerged in m-SBF for 7 days, b) results showing molar ratios of oxygen and magnesium, regions of approximate ratios of O to Mg indicated (dashed lines).

4.3 Calorimetry and pressure measurements

4.3.1 Exposure testing in NaCl solution

Figure 19 below shows the evolution of thermal power and pressure change rate in the three alloys of interest during exposure in 0.9 w-% NaCl. Alloys Z5 and ZX50 are tested for 48 hours, while alloy X0 for 24 hours. All three alloys have a spike in thermal power output when initially submerged, as a very small quantity of passivating MgO is formed from the atmosphere during the experiment start, and nearly-bare metal reacts readily with the solution. This is also seen in the initial pressure change. Afterwards, thermal output drops significantly in all three alloys. The X0 and ZX50 alloys then stabilize, while alloy Z5 start slowly increasing again. Similar trends were observed by Reinwalt and Tayeb-Bey, as discussed in section 2.4. However, their hypothesis that this increase would become extinct with time seems to be inconsistent with present experiment since thermal power output accelerates even after 24h.

A possible better explanation is that zinc-containing intermetallic particles separate from the matrix and react with water forming $Zn(OH)_2$. As can be seen in section 4.2.1, as the corrosion process proceeds, the surface area of the sample increases upon corrosion and the number of separated intermetallic particles increases. This would then increase the amount of zinc reacting with the solution forming a positive feedback loop, and the entire process accelerates. This also explains the rising pressure change rate. The hydroxylation reaction of zinc also releases hydrogen gas, and as the reaction of zinc accelerates, the pressure change rate increases linearly.

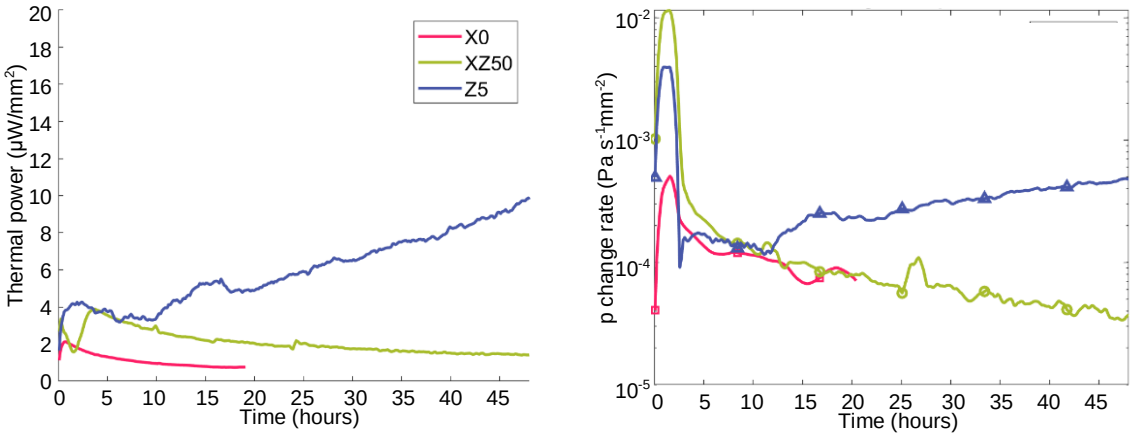

Figure 19: Thermal power and pressure change rate readings of X0, ZX50, and Z5 alloys in 0.9 w-% NaCl solution tested at 37°C for 48 hours (X0 only tested for approx. 20 hours).

In order to verify the assumption of the model that the majority of corrosion heat output correlates with the output of hydrogen gas, the derivatives of both the thermal power and pressure change rate can be compared, see figure 20.

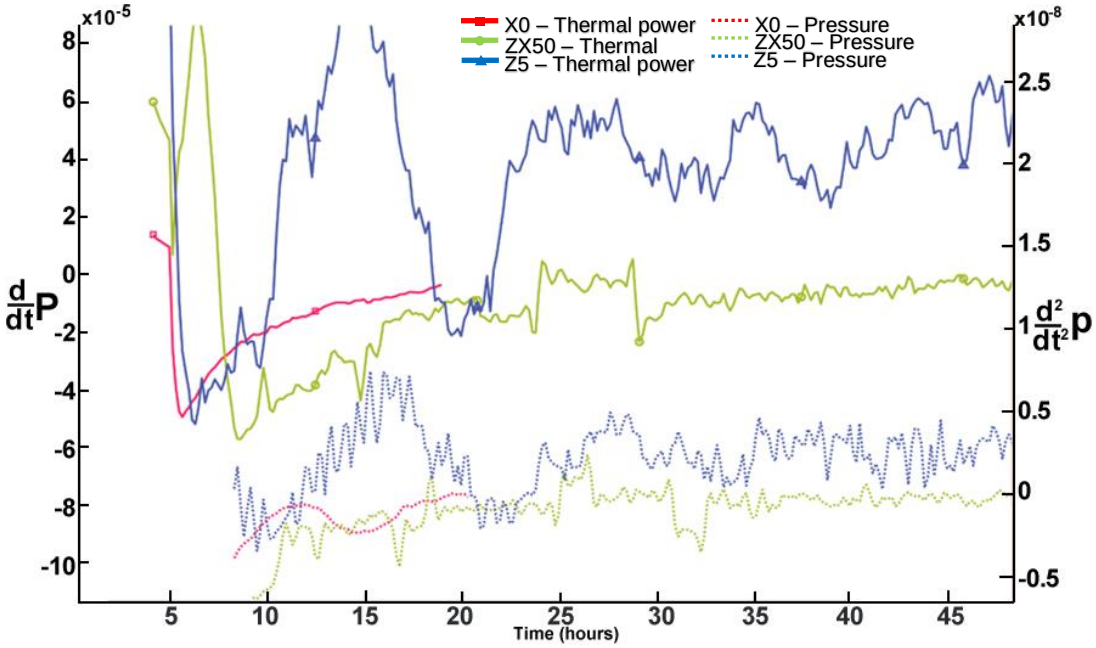

Figure 20: Derivatives of the results in figure 19. Derivative of thermal power (solid lines), and pressure change rate (dotted lines).

If the curves have the same trends, i.e. if a change in thermal power agrees with evolution in a pressure change rate, then the production of hydrogen does indeed correlate with heat generation. In figure 20, both the Z5 and ZX50 alloys exhibit very similar curves for both thermal power and pressure change rate, which suggests that the main reaction taking place is one that generates hydrogen, most likely magnesium reacting with water.

The X0 alloy however has a region between 12 and 17 hours where the curves do not overlap. This suggests the existence of an additional unknown reaction during this period.

Note that the initial hours of the readings have been omitted due to the high unstable state of the system.

4.3.2 Exposure testing in m-SBF

Figure 22 shows the evolution of thermal power and pressure change rate in the alloys during exposure in m-SBF for 48 hours. Similar to the tests in NaCl, an initial spike in thermal power and pressure change rate are observed at the start of the experiment, most likely due to the reaction of the nearly-bare metal surfaces. Both readings are significantly higher than during the test in NaCl, which is consistent with the literature. Z5 and ZX50 alloys no longer exhibit an accelerated thermal output, and the pressure change rate does not increase confirming the [absence of an] effect.

If the acceleration of corrosion is due to the formation of $Zn(OH)_2$, as suggested in section 4.3.1, then the lack of this effect in m-SBF can be explained by the presence of buffer since $Zn(OH)_2$ is only stable in alkaline solutions (Beverskog and Puigdomenech, 1997).

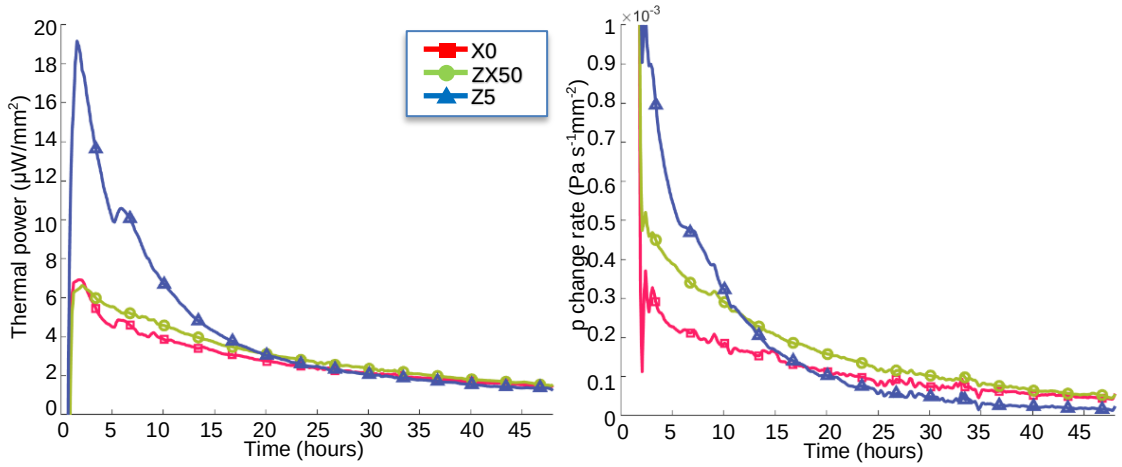

Figure 21: Thermal power and pressure change rate readings of X0, ZX50, and Z5 alloys in m-SBF, tested at 37°C for 48 hours.

Comparing the derivatives for these curves shows that they agree with the basic model assumption very well, see figure 22.

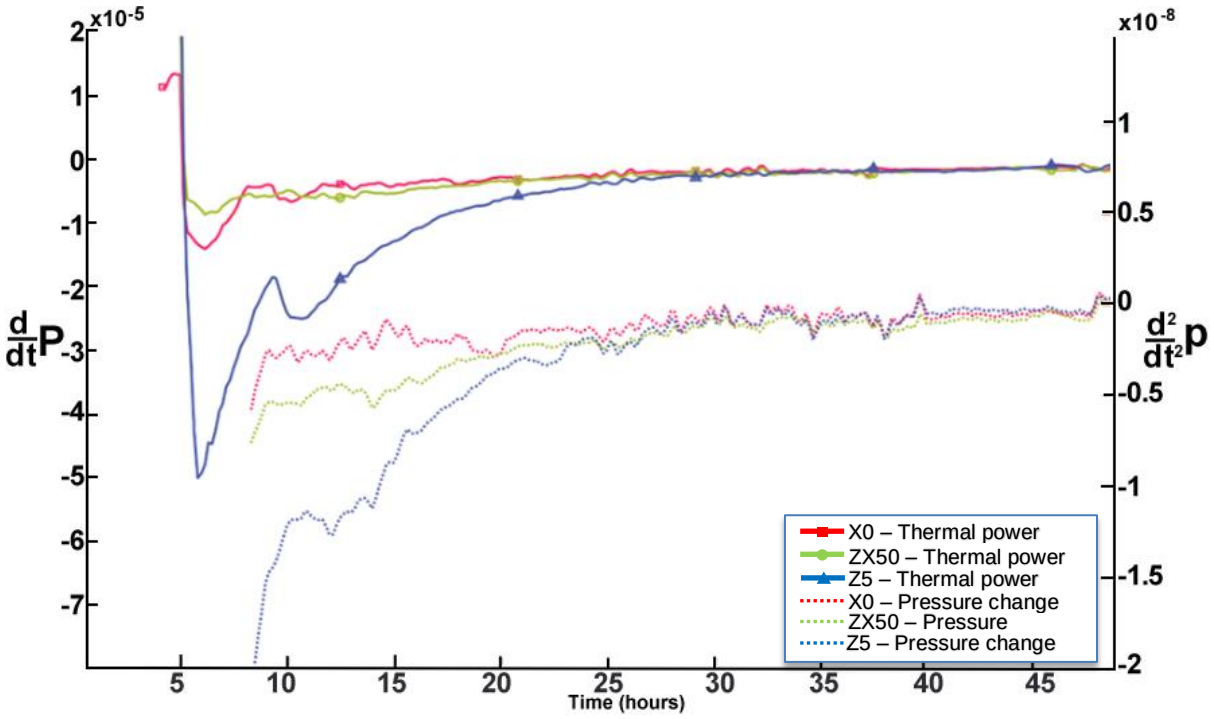

Figure 22: Derivatives of the results in figure 21. Derivative of thermal power (solid lines), and pressure change rate (dotted lines).

4.3.3 Exposure testing of heat-treated specimens in m-SBF

Heat treatment is expected to lower the thermal power output and pressure change rate due to the effect of solid solution, and this is observed indeed in figure 23 for all the alloys except Z5 heat treated at 420°C for 24h. The latter exhibits an increase in thermal power output and pressure change rate compared to the as cast sample.

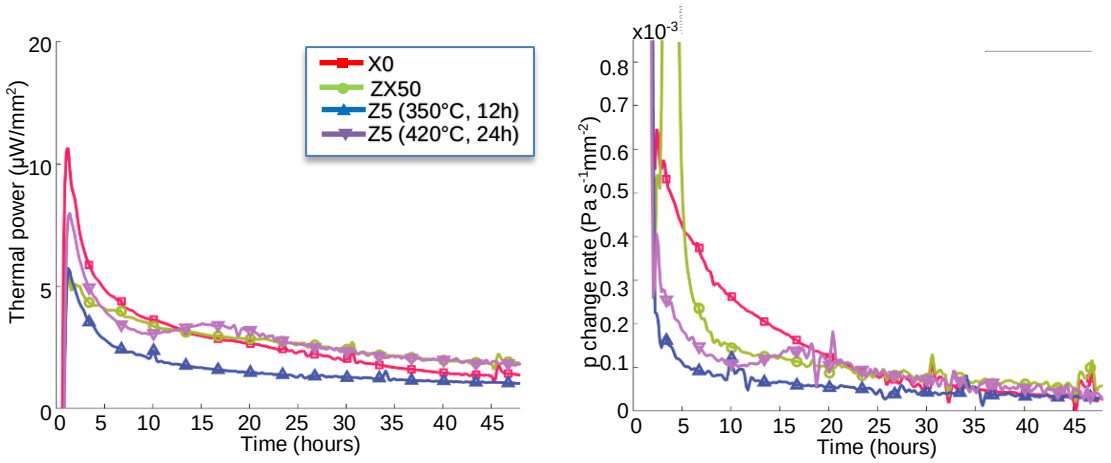

Figure 23: Thermal power and pressure change rate readings for heat treated X0, ZX50, and Z5 alloys in m-SBF, at 37°C for 48 hours.

Similar to figure 22, the analysis of the derivatives for these readings in figure 24 match very closely, again suggesting a strong correlation between heat output and hydrogen evolution.

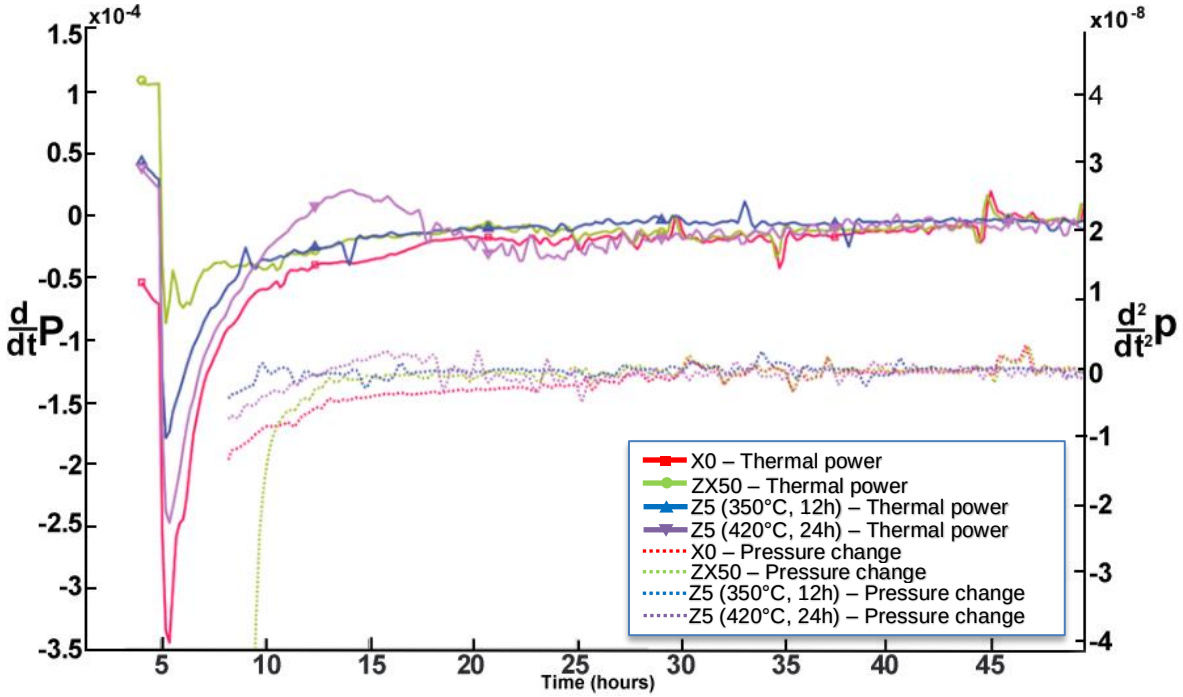

Figure 24: Derivatives of the results in figure 23. Derivative of thermal power (solid lines), and pressure change rate (dotted lines).

4.3.4 Corrosion rates and enthalpies

By utilizing equations (5) and (6), the evolutions of corrosion rate and enthalpy for all tested alloys can be calculated. Respective results are presented in figure 26. Firstly, the corrosion rates will be discussed. All the alloys show a spike in corrosion rate similar to that in the pressure change rate measurements, which is expected since corrosion rate is directly proportional to the pressure change rate. Again, this is primarily due to the reaction of nearly-bare metal surface upon contact with the corrosion medium. In addition, it takes some time for the calorimeter to reach stable operating conditions upon entering relatively large thermal bodies into the sensitive instrument at the start for the experiment.

For the alloy X0 in NaCl, corrosion rate quickly decreases after around four hours, and then stabilizes at approximately 2mm/year. The as-cast and SSSS specimens in SBF at first deviate, with the corrosion rate for the as-cast specimen being lower. However, after around 20 hours they converge at approx. 1mm/year.

The ZX50 alloy, similar to the X0 alloy, has the lowest corrosion rate in NaCl, with the SSSS specimen matching it after around 10 hours with a rate of ~2mm/year. The as-cast specimen exhibits a significantly slower decrease in corrosion rate, matching that of the SSSS specimen after 35 hours.

Z5 in NaCl has a relatively stable corrosion rate of about 1mm/year for 15 hours, after which it starts steadily climbing. As discussed in section 4.3.1, this might be due to a secondary reaction of Zn. The as-cast specimen in SBF initially has the highest corrosion rate of all Z5 specimens until 35 hours, after which it becomes the lowest. The SSSS specimen heat treated at 350°C for 12 hours exhibits a very stable and low corrosion rate of around 1mm/year, as expected, as this was theoretically optimal temperature for solid solution treatment. The specimen treated at 420°C for 24 hours has a higher corrosion rate with a temporary increase between 10 and 15 hours before decreasing again. The higher temperature of heat treatment may have resulted in incipient melting and the formation primary precipitates leading to local galvanic couples and thus accelerating corrosion rate.

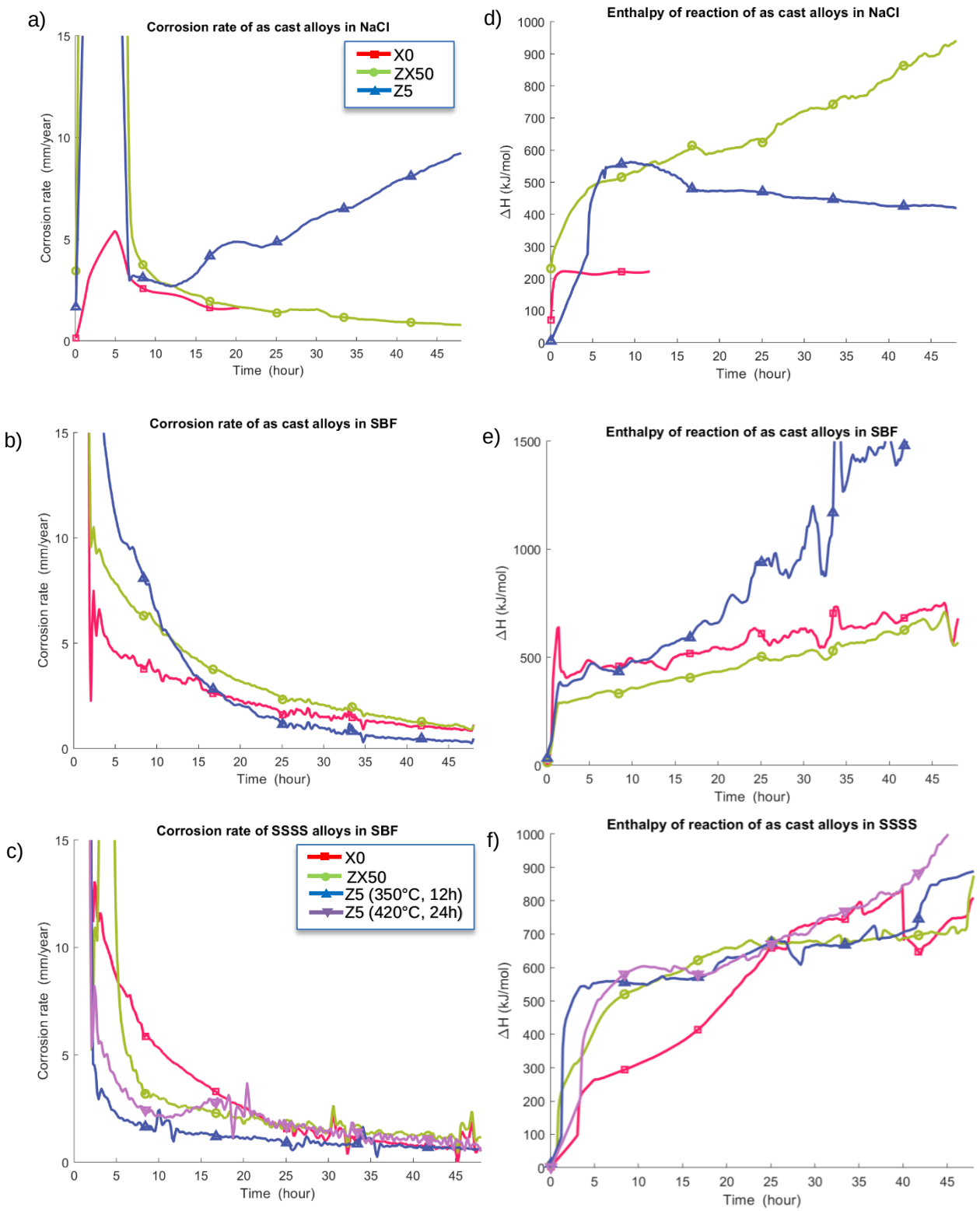

Figure 25: Change in corrosion rates (a-c), and enthalpies (d-f) over time for as cast and SSSS X0, ZX50, and Z5 alloys tested in NaCl and SBF at 37°C for 48 hours. Enthalpies are presented as absolute values, though as exothermic reaction enthalpies, they would be negative.

As described in section 2.1, the main reaction expected to occur is the direct reaction between Mg and H_2O with a reaction enthalpy of -353.01kJ mol^{-1}. Due to the low reliability of results in the beginning of an experiment, i.e. before the calorimeter reaches thermal equilibrium, the first two hours have been omitted. The as cast X0 alloy in NaCl does stabilize at lower value (approx. -250kJ mol^{-1}), but this could be due to potential pressure leaks in the experimental setup. The enthalpy of the ZX50 alloy reaches 500kJ mol^{-1} in the first 5 hours, and then increases linearly for the rest of the experiment. This increase could be due to $Mg(OH)_2$ starting to precipitate out as the medium becomes saturated with OH^- ions. The as cast Z5 alloy in NaCl reaches an enthalpy of around 550kJ mol^{-1} in the first 10 hours, and then slowly decrease again. This might be due to the potential bi-reaction of Zn discussed in section 4.3.1.

All the as-cast specimens tested in SBF show initial enthalpy of around 350kJ mol^{-1}, while ZX50 and X0 increase steadily to around 500 kJ mol^{-1} at the end of testing period. The Z5 alloy exhibits a much larger increase in enthalpy over time. The roughly linearly increasing trend could be attributed to various reactions forming calcium oxide-compounds, phosphates, apatite, etc. that have been reported to occur in SBF. Zn has been shown to facilitate the nucleation of apatite, which could explain the bigger increase in enthalpy.

The SSSS samples all show a very similar trend, starting at around 500kJ mol^{-1} and increasing to 800-900kJ mol^{-1}. The X0 alloy does start off much lower, at around 250kJ mol^{-1} but converges with the other samples after around 25 hours.

Z5 alloy in SBF did not exhibit the increase in corrosion rate that it did in NaCl during the 48 hour experiment, most likely due to the buffering salts present in SBF. However, at longer timescales, figure 27, the buffer may become depleted, and the same behaviour is observed, although to a lesser degree. The same is true for ZX50 alloy.

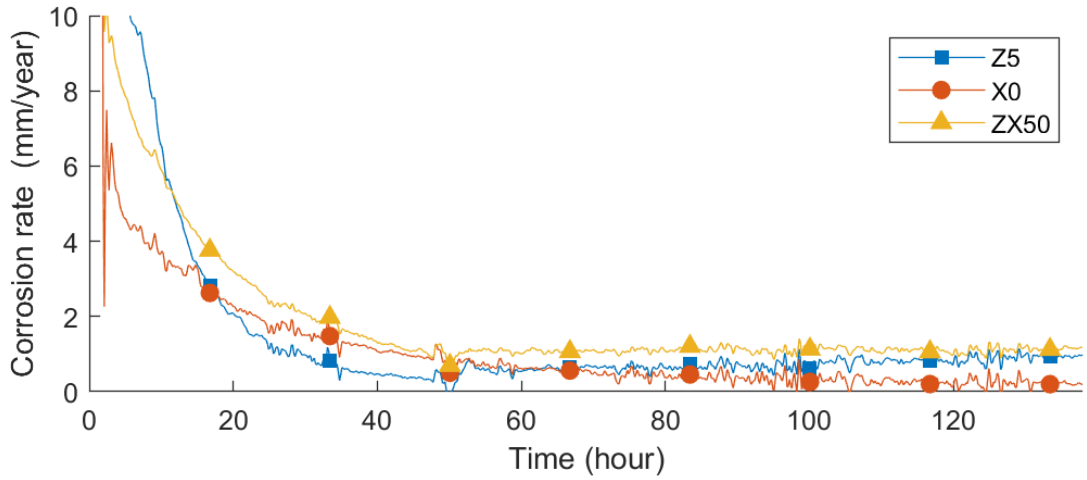

Figure 26: Corrosion rate for Z5, X0, and ZX50 as cast alloys in m-SBF, tested at 37°C for 140 hours.

4.3.5 Comparison of average corrosion rates

In figure 27, average corrosion rates after 24h for all the tests are compiled. For X0 and ZX50 alloys, the highest corrosion rate is seen in m-SBF, as cast. The Z5 alloy has a very high corrosion rate in NaCl, which decreases dramatically when tested in m-SBF. This is likely due to the hydrogen evolution of the $Zn(OH)_2$ reaction discussed in section 4.3.1. As this reaction does not seem to take place in m-SBF, this effect is not present and corrosion rate is considerably lower.

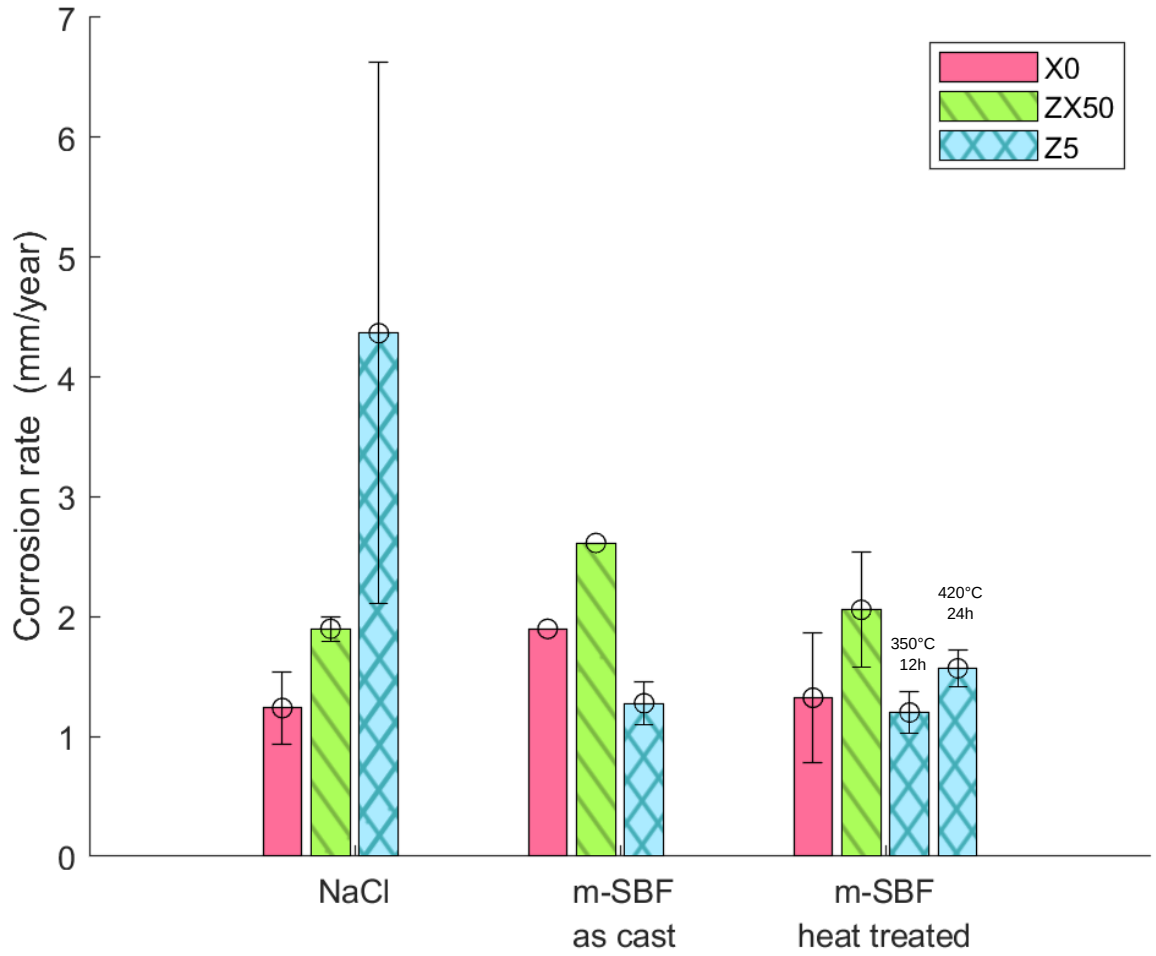

Figure 27: Average corrosion rates of as cast and SSSS X0, ZX50, and Z5 alloys, tested in NaCl and SBF at 37°C after 24h.

Heat treatment of the samples improves corrosion resistance but only precipitously. The Z5 alloy heat treated at 420°C shows an increased corrosion rate. This is likely due to the presence of eutectics leading to partial melting of the alloy, in-turn resulting in local liquid phases that do not disperse before quenching. There would then be local galvanic coupling at these sites accelerating corrosion rate.

The average corrosion rates after 48 hours are presented in figure 28 for all specimens except X0 in NaCl. The average corrosion rate decrease for all the specimens apart from Z5 in NaCl, as compared to the averages after 24 hours. While the as cast X0 alloy in SBF has a lower average corrosion rate than ZX50 after 24 hours, after 48 hours their average corrosion rates are almost identical. After 24 hours the SSSS Z5 specimens heat treated at 350°C show a lower average corrosion rate than that of the specimens treated at 420°C, and after 48 hours the picture reverses.

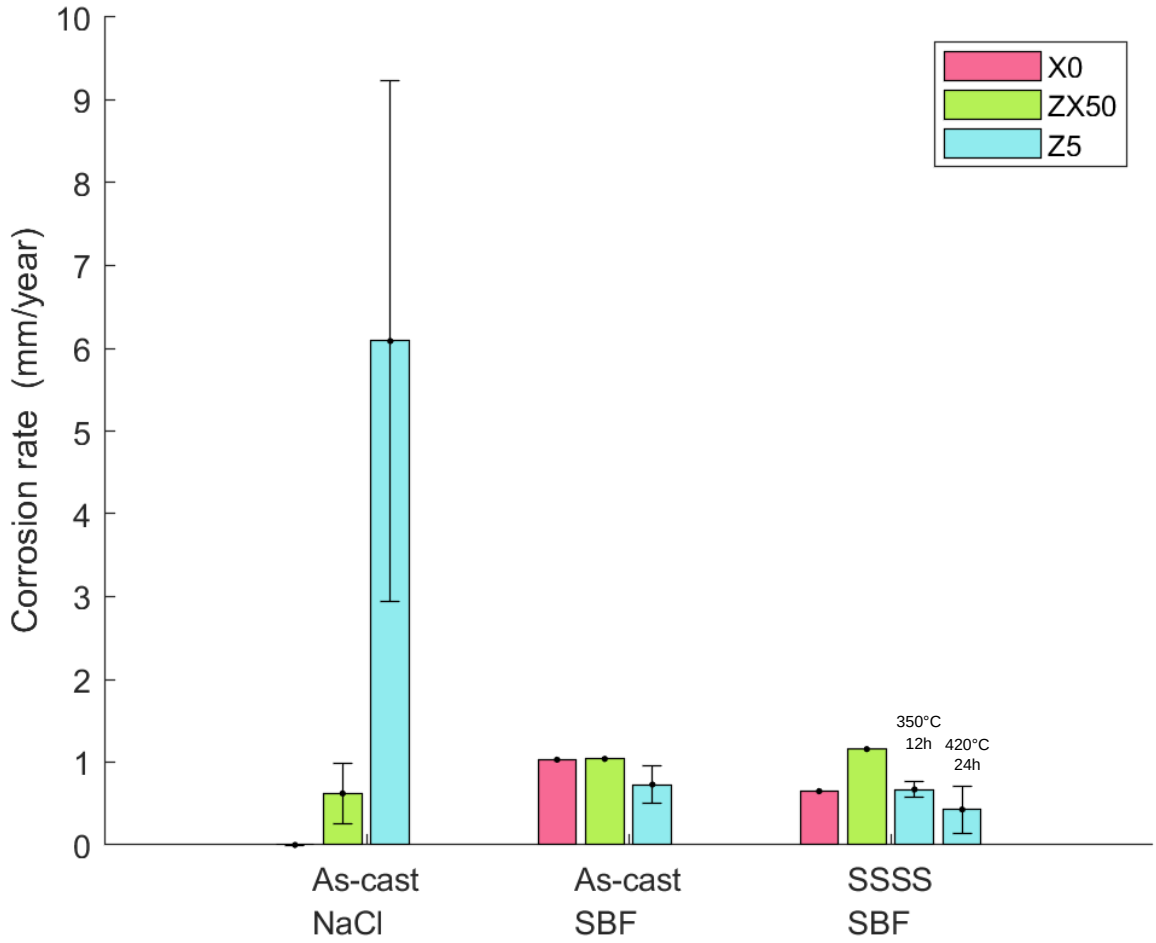

Figure 28: Average corrosion rates of as cast and SSSS X0, ZX50, and Z5 alloys, tested in NaCl and SBF at 37°C after 48h (Data for X0 in NaCl not available).

4.4 pH-levels and heat output

To see whether the point where the pH stabilizes and allows $Mg(OH)_2$ to form influences the thermodynamics of the system, pH change over time are measured at the same conditions as the calorimetric measurements. First, pure Mg is tested, as the approximate time for equilibrium to occur (approx. 4-5 hours) have been reported in the literature. Respective results are presented in figure 29.

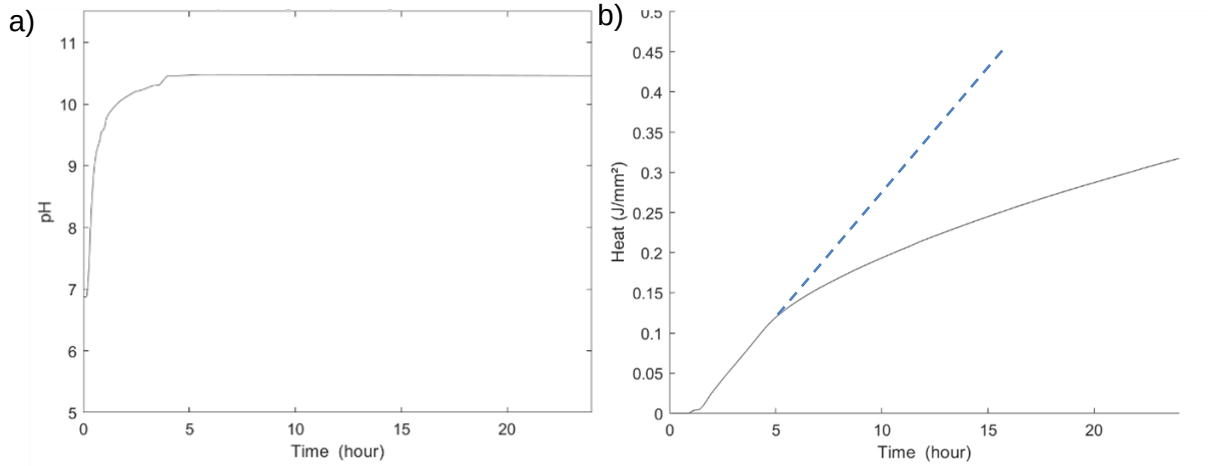

Figure 29: a) evolution of pH factor of test medium, with pure Mg tested in NaCl solution, b) heat output of reaction of pure Mg in NaCl solution, with measured results (solid line), and extension of linear region (dashed line).

The pH does indeed stabilize near 10.5 after around four and a half hours. The evolution of heat increases linearly until the same time as the pH saturation, and then exhibits a change to a logarithmic dependence. The linear region has been extended with a dotted line in figure 29 to highlight the difference. This would suggest that the formation of $Mg(OH)_2$ has an effect on the reaction kinetics of the system.
After the observation of such a behaviour, it was decided to test the alloys. The results for as cast Z5 alloy are presented in figure 30.

The pH level stabilizes at slightly below 10.5 after approximately 5 hours. While the effect is significantly less pronounced, the slope of the heat evolution does change at this point of time. However, at around 15 hours it reverts to a linear increase, surprisingly with a steeper slope than during the initial test period. The 15 hour mark also corresponds to the start of thermal power increase in figure 21. As discussed in that section, this could also be attributed to the potential secondary reaction of Zn.

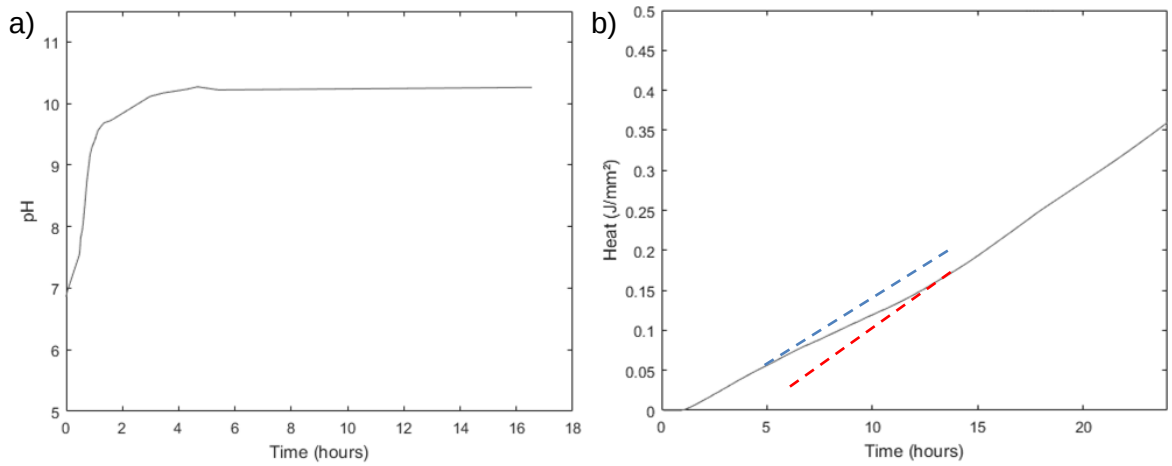

Figure 30: a) evolution of pH factor of test medium, with Z5 tested in NaCl solution at 37°C, b) heat output of reaction of Z5 in NaCl solution at 37°C, with measured results (solid line), and extension of linear regions (dashed lines).

5. Conclusions

This project examined Mg alloys with Zn and Ca for potential use in bio-medical implants. In particular, the influence of solid solution treatment and immersion medium on corrosion rate were investigated. Isothermal calorimetry, pressure measurements and SEM with EDS were used for evaluating material corrosion rates and the build-up of corrosion products.

Corrosion medium is found to greatly affect the corrosion of all three alloys. While corrosion rates were lower for X0 and ZX50 alloys in NaCl than m-SBF, the corrosion rate of Z5 alloy was dramatically reduced in m-SBF.

Solid solution treatment improves the average corrosion rate after 24 hours in all the alloys when heat treated at an optimal temperature. SSSS Z5 alloy heat treated at 350°C for 12h exhibits the lowest corrosion rate.

After 48 hours the average corrosion rates continued to decrease except for as cast Z5 alloy in NaCl. The alloy exhibiting the lowest average corrosion rate after 48 hours is the SSSS Z5 alloy heat treated at 420°C for 24 hours.

The saturation of pH seems to affect the reaction kinetics of the samples, with the kinetics being linear before saturation and logarithmic afterwards. For Z5 alloy, the kinetics return to linear after 15 hours, at which point the alloy corrosion rate starts increasing.

References

Aghion, E. and Bronfin, B. (2000). Magnesium Alloys Development towards the 21st Century. *Materials Science Forum*, 350-351, pp.19-30.

Barbeck, M., Serra, T., Booms, P., Stojanovic, S., Najman, S., Engel, E., Sader, R., Kirkpatrick, C., Navarro, M. and Ghanaati, S. (2017). Analysis of the in vitro degradation and the in vivo tissue response to bi-layered 3D-printed scaffolds combining PLA and biphasic PLA/bioglass components – Guidance of the inflammatory response as basis for osteochondral regeneration. *Bioactive Materials*, 2(4), pp.208-223.

Beverskog, B. and Puigdomenech, I. (1997). Revised pourbaix diagrams for zinc at 25–300 °C. *Corrosion Science*, 39(1), pp.107-114.

Esmaily, M., Svensson, J., Fajardo, S., Birbilis, N., Frankel, G., Virtanen, S., Arrabal, R., Thomas, S. and Johansson, L. (2017). Fundamentals and advances in magnesium alloy corrosion. *Progress in Materials Science*, 89, pp.92-193.

Ghali, E. (2011). Activity and passivity of magnesium (Mg) and its alloys. *Corrosion of Magnesium Alloys*, pp.66-114.

Liu, X., Yin, M., Zhang, S., Wei, H., Liu, B., Du, H., Hou, L. and Wei, Y. (2018). Corrosion Behavior of the As-Cast and As-Solid Solution Mg-Al-Ge Alloy. *Materials*, 11(10), p.1812.

Oyane, A., Kim, H., Furuya, T., Kokubo, T., Miyazaki, T. and Nakamura, T. (2003). Preparation and assessment of revised simulated body fluids. *Journal of Biomedical Materials Research*, 65A(2), pp.188-195.

Perrault, G. (1974). The potential-pH diagram of the magnesium-water system. *Journal of Electroanalytical Chemistry and Interfacial Electrochemistry*, 51(1), pp.107-119.

Song, G. (2011). Corrosion electrochemistry of magnesium (Mg) and its alloys. *Corrosion of Magnesium Alloys*, pp.3-65.

Staiger, M., Pietak, A., Huadmai, J. and Dias, G. (2006). Magnesium and its alloys as orthopedic biomaterials: A review. *Biomaterials*, 27(9), pp.1728-1734.

UNITIKA Plastics Division. (2020). *Chemical Resistance ／UNITIKA Nylon 6 ／Nylon Resin ／Producs ／UNITIKA Plastics Division*. [online] Available at: https://www.unitika.co.jp/plastics/e/products/nylon/nylon6/07.html [Accessed 28 Jan. 2020].

Wadsö, L 2005, 'Applications of an eight-channel isothermal conduction calorimeter for cement hydration studies', *Cement International*, vol. Jg. 3, no. Nr 5, pp. 94-101.

Wadsö, L., Hort, N. and Orlov, D. (2019). Effect of Alloying with Rare-Earth Metals on the Degradation of Magnesium Alloys Studied Using a Combination of Isothermal Calorimetry and Pressure Measurements. *The Minerals, Metals & Materials Series*, pp.121-126.

Waugh, D. and Lawrence, J. (2010). Wettability analysis of CO2 laser surface patterned nylon 6,6 samples soaked in simulated body fluid (SBF). *Proceedings of the 36th International MATADOR Conference*, pp.465-468.

Witte, F., Kaese, V., Haferkamp, H., Switzer, E., Meyer-Lindenberg, A., Wirth, C. and Windhagen, H. (2005). In vivo corrosion of four magnesium alloys and the associated bone response. *Biomaterials*, 26(17), pp.3557-3563.

Appendix 1

Matlab code used for data reduction and analysis

```
%% Isothermal Calorimeter Pressure and Thermal Power Analysis
%% Description

% Date Created: Summer 2018
% Last Updated: 25-07-2019 (Ilyes Tayeb-Bey)
%               27-11-2019 (Max Viklund)
% Developed by: Lars Wadso

% This script imports the plw files take from the calorimeter, calculates
% mean values, and graphs the averaged data in the following graphs:
    % Thermal power (P)
    % Heat (Q)
    % Pressure change (p)
    % dp/dt
    % Corrosion rate (dn/dt)
    % Enthalpy variation (dH)
clear all;
close all;

  [n, s] = xlsread('SampleDatabase.xlsx', 'A12:G12'); % n reads area, and s
text. Choose row of data with AX:GX

    date = char(s(1,1));    % Date of experiment
    desc = char(s(1,2));    % Description of experiment
    fil = char(s(1,3));     % Filename

    % cal = [7.4419  7.6615  7.4659  7.2696  7.6536  7.5899  7.3643
7.4409];  % TAM AIR 4 Calibration coefficients Units:mW/mV
    % BL = [0.00256394851021469 0.00566411111503840 0.00942984689027071
0.00364753417670727 -0.304956287145615 0.00944369938224554
0.0105007505044341 0.0175819955766201]; % Baseline values for TAM Air 4
Units: mV

    cal = [7.4419  7.4659  7.5899 7.4409];  % TAM AIR 4 Calibration
coefficients Units:mW/mV (Only for channels 1,3,6,8)

    BL = [0.00256394851021469 0.00942984689027071 0.00944369938224554
0.0175819955766201]; % Baseline values for TAM Air 4 Units: mV (Only for
channels 1,3,6,8)

    pCal = [42.54 43.27 42.95 43.36]; % Pressure calibration sensor Units:
Pa/mV

   [t,Volt]=PLW2ML(fil);
    k=[1,3,6,8:12];
    U(:,1:8) = Volt(:,k);

    figure;clf % Creates figure window
%% Thermal power average

%    subplot(321);hold oo
        N=60; % Mean over 10min, number of data points to average over
     dt = t(2)-t(1);
     for k=1:4
```

```
          for kk=1:length(t)/N
              Pav(kk,k)=mean(U((1:N)+(kk-1)*N,k)); % Mean values of rate
          end
      end
%% Pressure average
      for k = 5:8
          qq = U(1:N:end,k);
          Pav(:,k)=qq(1:end-1);   % Values of pressure       if bug at this
line just replace  [ qq(1:end)] by [ qq(1:end-1) ]
      end
      U = Pav;
      t=((0:dt*N:t(end))+dt*N/2);
      if length(t)>length(U);t(end)=[];end
      if length(t)<length(U); t(end+1)=t(end)+diff(t(end-1:end));end
      dt = t(2)-t(1);

%% P Thermal power

% Plots Thermal power
     subplot(321);hold on
    for k = 1:4
        P(:,k) = ((U(:,k) - BL(k)) * cal(k))/n(k)*1000; % Thermal power
(uW/mm²)
        plot(t/3600 , P(:,k),'.')
%         plot(t(1:end-1)/3600 , P(:,k),'.')
    end

% Sets axes
    hold off
    axis([0 t(end)/3600 0 8]);
    xlabel('Time  (hour)');
    ylabel('Thermal power (\muW/mm²)');
    legend('Sample 1','Sample 2','Sample 3','Sample
4','location','NorthEast');

 %% Q Heat

 %  Plots Heat
 subplot(322);hold on
 PP=[];
     for k = 1:4
         QP(:,k)=P(:,k);
         QP(1:round(360/N),k)=0; %removing first 2 h
         Q(:,k)=(cumsum(QP(:,k))*dt/1e6); % Heat  (J/mm²)
         plot(t/3600,Q(:,k),'.')
%         plot(t(1:end-1)/3600,Q(:,k),'.')
     end
     disp(' ')
     hold off

  % Sets axes
     ylabel('Heat (J/mm²)');
     axis([0 t(end)/3600 0 max(Q(:))*1.2]);
     xlabel('Time  (hour)');
     %legend('Sample 1','Sample 2','Sample 3','Sample
4','location','NorthWest');

 %% p Pressure change
```

```
%  Plots pressure change
    subplot(323);hold on
    for k = 5:8
        p(:,k)=((U(:,k) - U(2,k))*pCal(k-4)/1000)/n(k-4); % zero at the
beginning of the experiment
        plot(t/3600,p(:,k),'.') % Pressure change (kPa/mm²)
%       plot(t(1:end-1)/3600,p(:,k),'.')
    end

    hold off

% Sets axes
    ylabel('Pressure change  (kPa/mm²)');
    xlabel('Time  (hour)');
    %legend('Sample 1','Sample 2','Sample 3','Sample
4','location','NorthWest');
    axis([0 t(end)/3600 0 0.05])

 %% dp/dt

% Plots dp/dt
   subplot(324);hold on
   WindowSize=10;   % Filter value
   b = ones(1,WindowSize);    a=sum(b);% Filter

    for k = 5:8
        dpdt(:,k)=filter(b,a,gradient(p(:,k))/dt*1000); %Filter

        plot(t/3600,dpdt(:,k),'.') % dp/dt (Pa/(s.mm²))
%       plot(t(1:end-1)/3600,dpdt(:,k),'.')
    end
    hold off

% Sets axes
    xlabel('Time  (hour)');
    ylabel('{\it p} change rate  (Pa.s^{-1}.mm^{-2})');
    %legend('Sample 1','Sample 2','Sample 3','Sample
4','location','NorthEast');
    axis([0 t(end)/3600 0 0.001])

     %% Corrosion rate


    subplot(325);hold on
    V=(135.4-17)*1e-6;          %(1 small and 1 big vial) (m^3)
    R=8.314;                  % Gas constant J/(K.mol)
    T=310;                    % Experiment temperature (K)
    MMg=24.305*1e-3;             % Molar mass of Mg (kg/mol)
    den=1740*1e-9;                    % Density of Mg (kg/mm3)

    for k = 5:8
            dpdtx(:,k)=dpdt(:,k);          % dp/pt for one specimen
            dndtx(:,k)=dpdtx(:,k)*V/R/T;  % Corrosion rate (mol/(s mm2)
            dndt(:,k)=dndtx(:,k)*4.40e11;
          rate(k-4) = mean(dndt(144:145,k));
            plot(t/3600,(dndt(:,k)),'.')
%           plot(t(1:end-1)/3600,(dndt(:,k)),'.')
    end
%     rate=mean(rate(1:3));
```

```
% Sets axes
    xlabel('Time (hour)');
    ylabel('Corrosion rate  (mm/year)');
    %legend('Sample 1','Sample 2','Sample 3','Sample
4','location','NorthEast');
    axis([0 t(end)/3600 0 5])


      %% dH

  %  Plots Enthalpy Variation (DeltaH) and rate corrosion (dn/dt)
    subplot(326);hold on

    for k = 1:4
         dH(:,k)=P(:,k)/1000./(dndtx(:,(k+4))*1e6); % J/s / mol/s = J/mol
         plot(t/3600,dH(:,k),'.')           % Enthalpy variation (kJ/mol)
%        plot(t(1:end-1)/3600,dH(:,k),'.')
    end

    hold off

% Sets axes
    xlabel('Time (hour)');
    ylabel('\DeltaH (kJ/mol)');
    %legend('Sample 1','Sample 2','Sample 3','Sample
4','location','SouthEast');
    axis([0 t(end)/3600 0 1000])

%% finish
% Sets figure size proportions and title
set(gcf,'units','centimeters','position',[2 2 30 12],'color','w');
title = annotation('textbox', [0 0.9 1 0.1], 'String', [date ' ' desc],
'EdgeColor', 'none', 'HorizontalAlignment', 'center');
title.FontWeight = 'bold';
title.FontSize = 12;
```

Appendix 2

Results of pH-measurements

Pure Mg in NaCl

t(s)	pH
0	6,881
360	6,869
600	6,885
780	7,076
840	7,165
900	7,26
960	7,35
1020	7,46
1080	7,625
1140	7,86
1200	8
1260	8,01
1320	8,22
1440	8,4
1500	8,5
1740	8,85
1980	9,068
2220	9,222
2460	9,308
2760	9,388
2820	9,42
3060	9,55
3300	9,569
3600	9,611
3900	9,763
4320	9,844
4800	9,902
5400	9,97
6120	10,04
7200	10,112
8760	10,199
9600	10,221
9960	10,229
11820	10,298
12960	10,31
14160	10,45
20100	10,478
86400	10,46

Z5 in NaCl

t(s)	pH
0	6,856
120	6,945
1680	7,54
1740	7,6
1800	7,7
1860	7,828
2040	7,921
2160	8,039
2400	8,365
2640	8,726
3060	9,167
3300	9,29
3720	9,42
4080	9,564
4800	9,682
5760	9,727
10740	10,116
12480	10,172
15360	10,23
16800	10,271
19500	10,221
59580	10,262

LUNDS UNIVERSITET